# Observations of shoaling and breaking waves in shallow water with different coherent X-band radars

Susanne Støle-Hentschel, Patricio A. Catalán, Michael Streßer, Jochen Horstmann and Frédéric Dias

***Abstract*—The study analyzes the microwave imaging of shoaling nearshore surface gravity waves during the process of steepening and breaking over two beaches for a wide range of environmental conditions. Data are sourced from two coherent X–band radars, operating under low grazing angle conditions. Using automatic wave tracking on the radar images, the evolution of individual waves is followed over hundreds of meters. The extracted backscatter intensity and Doppler speed form distinct patterns that reveal a non-negligible dependence on environmental conditions. Statistical representations of the backscattered signal are presented by conditional Doppler speed–Intensity histograms. These are composed of ensembles extracted at the radar-facing fronts. This technique helps to focus on the steepening of the wave and minimizes the impact of extremely low-grazing angle imaging mechanisms which are still not well understood. The combination of wind speed and direction as well as initial wave steepness, local depth, and degree of non-linearity contribute to the shapes and centroid positions of the histograms. The backscatter signature exhibited by breaking waves remained consistent and similar throughout all datasets. The results are consistent across radars. Before consolidating the findings, it is imperative to conduct a further investigation of radar imaging of non-linear wave dynamics in shallow water to eliminate any possible influence of imaging mechanisms.**

***Index Terms*—Coherent X-band radar, shallow-water wave evolution, wave breaking, wave tracking**

## I. Introduction

BREAKING waves in the nearshore play a vital role by dissipating wave energy, transferring momentum to mean flows and levels, thereby contributing to sediment transport, and shaping coastal morphology. As waves approach shallower waters, they shorten and steepen until they break. In the course of this process their energy transforms into turbulent kinetic energy that influences sediment movement and induces wave-induced currents, and entails coastal erosion or accretion. Additionally, breaking waves introduce air into the water, promoting aeration and oxygenation of coastal ecosystems.

One of the open research questions is defining how the prevailing environmental conditions impact the onset of wave breaking and energy dissipation. The majority of studies on wave breaking have been conducted based on simulations and laboratory experiments. Examples of simulation studies include the definition of a universal breaking criterion [1] or a scaling law of the dissipated energy for waves over a sloping beach [2] and the effect of wind on the cross-sectional shape of the wave [3]. A number of laboratory and field studies have expounded how the shape of the overturning wave relates to the generation of turbulence [4], [5], sea spray [6] and submerged bubbles [6]–[8]. Secondary effects like wave loads on structures [9] and sediment transport [10] also depend on the shape of the wave (e.g. the difference between surging and plunging breakers). The width-length ratio of the air cavity prior to the development of the wave roller has been demonstrated as the determining factor for characterizing the breaking intensity of breakers, ranging from gentle to extreme plunging [11]. More accurate shape measurements made available by lidars (e.g. [12], [13]) confirm this work and visualize how a steep wave starts to break, forms an air cavity that then changes shape, size and tilt during the breaking event [12]. While O'Dea et al. [12] found correlations of the breaker shape to the local beach slope, the effective depth, and the wave steepness just before breaking, Feddersen et al. [13] revealed different roller shapes under onshore and offshore wind conditions. Most of those studies emphasize

S. Støle-Hentschel is with the Université Paris-Saclay, ENS Paris-Saclay, Centre Borelli, Gif-sur-Yvette, France

P. A. Catalán is with the Universidad Técnica Federico Santa María, Departamento de Obras Civiles, Valparaíso, Chile

M. Streßer and J. Horstmann are with the Helmholtz-Zentrum hereon, Coastal Ocean Dynamics, Geesthacht, Germany

F. Dias is with the Université Paris-Saclay, ENS Paris-Saclay, Centre Borelli, Gif-sur-Yvette, France and the University College Dublin, School of Mathematics and Statistics, Belfield, Ireland

*corresponding author: S. Støle-Hentschel* (e-mail: sstolehe@ens-paris-saclay.fr)

on the overturning event itself and neglect the evolution and how the overturning shape arises from the initial incoming wave. In addition, the collected data sometimes suffers from a limited variability in environmental conditions that can possibly affect the drawn conclusions. It would be desirable to be able to collect more data systematically.

Marine radars could be suited for this task. They offer a unique advantage due to their large area of coverage and ability to operate over long time periods in most weather conditions. It is assumed that Bragg theory can be applied and that tilt modulation is the dominant imaging mechanism, the backscatter amplitude is strongly related to the local steepness of the waves (e.g. [14], [15]). Therefore, radars could be ideal for relating prior research on wave shape near the breaking point to a more global setting. However, before the full potential of radars can be exploited, possible influences of the imaging mechanism on the results have to be excluded as to validate the assumption.

Observations and modeling of wave breaking by radars date back multiple decades, and under a wide range of regimes and conditions. Not only the environmental conditions can change (wave heights and periods, as well as relative water depth, and wind), but also experimental settings (microwave wavelength, radar incidence and azimuthal angles) and processing techniques. There is a large body of literature focusing on the effect of low-grazing-angle measurements for waves in deep water regime (Lewis and Olin (1980), Phillips (1988), Smith et al. (1996), Hwang et al. (2008) [16]–[19]), shallow water studies (Poulter et al., 1994, Haller and Lyzenga, 2003, Catalán et al., 2014 and Streßer et al., 2021 [20]–[23]), theoretical work (Wetzel, 1986 [24]) and measurements in the laboratory (Melville et al., 1988, Ericson et al., 1999, Sletten et al., 2003, [25]–[27]). The main conclusion is that breaking waves lead to an increase in radar backscatter intensities and the presence of a fast peak in and the broadening of the Doppler spectrum. The reason why is not definitive nor a unique characteristic of breaking waves. For example, non–breaking waves can also have high backscatter intensities [22]. Breaking prompts a rapid change in backscattering mechanisms or involves several families of scatterers within the radar observation footprint ( e.g. Lewis and Olin (1980) [16] and Catalán et al. (2011) [28]), which obfuscates the interpretation.

Many studies have been conducted to understand microwave ocean backscatter observed with scatterometers ( [16], [29]–[31], to list only a few). Basic scattering models were developed thereof and are still widely in use particularly in the field of space- and air-borne remote sensing [32]–[34]. In recent years, satellite Doppler scatterometry for ocean observations has received increasing attention and new backscatter models aiming to extract geophysical information from the Doppler signal have been developed [35]–[37]. Most backscatter models fall back on statistical descriptions of the waves both for the waves' hydrodynamics and for wave breaking occurrence even if they were derived mostly considering phase-resolving wave quantities (e.g. [36], [38], [39]). The mentioned studies focus on waves in intermediate depth or deep water where wave shapes were initially approximated by linear theory for mid incidence, although the inclusion mutltiscale non-linear models has shown promise to explain features at low-grazing angles [40], [41], even in the absence of wave breaking. Wave breaking (whitecapping) is steepness-induced resulting in short lifespans and areal extent. In the nearshore, the water depth and thus wave statistics can change rapidly and over short distances limiting bulk spectral descriptions of the wave field and its resulting backscatter. Wave physics in the nearshore are fundamentally different as shoaling gradually increases the non-linearity of the waves by the simultaneous occurrence of shortening wavelengths and increase in wave amplitude. Wave shapes are often vertically skewed with short, very steep (or even breaking) fronts and long gently sloping rear sides. Wave fronts may steepen to the point where the horizontal distance between their crest and trough can become almost vertical, therefore smaller than the radar resolution cell. In addition, the depth-limited breaking alters the ocean surface over large areas and for an extended period. Consequently, regions of extremely high backscatter are followed by enlarged regions of very weak return which can lead to misinterpretations of the backscatter behind the wave crests [23].

In addition to the discrepancy in the wave physics, most nearshore observations correspond to the high incidence regime (conversely, low grazing angle), where the look direction becomes almost tangential to the mean sea surface. Bragg-scattering

and composite surface theory [32], [42] are only validated for moderate incidence (grazing angles of $20° - 80°$). Under the extreme grazing regime, additional sources of scattering become significant, e.g. bound waves [30], non-linear surfaces or scattering from bores or small scale breaking waves [43].

Despite of these apparent limitations, a wide range of applications for marine radar data exist. Holman and Haller (2013) offer a summary and review of the challenges in establishing the relation between backscatter and geophysical variables [44]. These applications do not require a profound understanding of the imaging mechanisms. This may hold for processes that are sufficiently long when compared to the sampling time (e.g. rip currents, currents, hydraulic jumps and plumes, or geomorphological features) where phase averaging or other statistical approaches can be called upon to enhance the signal to noise ratio of the process of interest. For example, some applications rely on the radar's ability to measure the dispersion relation to estimate currents and bathymetry [45]–[49]. Others extract discernible signatures to detect wave breaking [28], wave breaking dissipation [50], [51], velocity fields [52], [53], rip currents [54], as well as subsurface features present in estuaries such as internal hydraulic jumps [55], buoyant plumes [56], [57]. However, phase resolving attempts are more difficult, owing to the high variability and sometimes short duration of the backscatter signatures and/or short lifespan or small areal coverage of the scatterers. These include, for instance, interferometry to retrieve free surface elevation fields [58]. A thorough understanding of the imaging mechanism is thus required for this particular environment.

Yet only a handful of studies have focused in understanding the backscatter characteristics of surfzone waves. While collected from a nearshore setting, some studies focused on steepness-limited waves away from the surf zone ( [16], [18], [20], [59]–[62]) or using other microwave bands, such as S-band ( [18], [20], [63]) or L-band [64]. Studies in the X-band focusing on nearshore wave scattering include Haller and Lyzenga [21], albeit at mid-grazing incidence; low-grazing-angle collected by Puleo et al. [52] using the Focused Phased Array Imaging Radar (FOPAIR, [65]) that has also been employed in the studies of Farquharson et al. [58], [66]; and studies relying on the same marine radars as used herein, although restricted to a few specific cases or environmental conditions ( [22], [23]). Comparative studies across data and radar systems have not been published to date.

The present work is a first step towards closing this gap. It demonstrates new analysis techniques that provide insight on the evolution of nearshore waves as they undergo non-linear changes induced by changing shallow bathymetry. Three key points distinguish the analysis from previous work:

1) The data presented covers an unparalleled range of environmental conditions collected during three independent field campaigns at two distinct sites. To capture the influence of the environmental conditions on the wave kinematics, the Doppler speed values were normalized according to the expected governing speeds of the observed scatterers: wave phase speed for breaking waves and maximum orbital speed for non–breaking waves.
2) Limiting the analysis to the well-illuminated wave fronts simplifies the interpretation of the backscatter. This avoids challenging radar imaging effects related to observing steep and breaking waves at a low grazing angle compounded by radar pulse smearing and shadowing [23].
3) Shoreward-traveling waves are tracked automatically over extensive distances, granting exclusive insight into the evolution of local steepness and Doppler speeds under varying environmental circumstances.

The description of radar systems, field conditions, and analysis methods can be found in Section II. Section III-A presents an overview of the radar return for various sea states, including the effects of wind conditions, wave steepness, relative depth, and degree of non-linearity. Section III-B then analyzes the evolution of Doppler speed and intensity as individual waves shoal for different sea states. The discussion in Section IV examines the outcomes in relation to earlier research, system settings, and processing methods.

The backscatter analysis for diverse environmental conditions provides a groundwork for advancing backscattering models suitable for microwave radar usage under low-grazing conditions in the nearshore. By capturing the evolution over large distances, the presented methods offer insight on the impact of wind and sea conditions on the wave kinematics, i.e. those of the gravity waves during

their transition form the outer surf zone towards the shore.

## II. Data and Methods

The present study compares datasets obtained using two different pulsed coherent radar systems: a fully coherent system called RiverRad [67], and a coherent on-receive system called Hereon radar [68]. The datasets were recorded at the same beach at the Field Research Facility (FRF) in Duck (NC, USA) but in different years, while the third dataset was recorded at Sylt island (Germany). The radar installations were partly already described in previous works, i.e. RiverRad at the FRF [22], [28] and Hereon radar at Sylt [23], [51]). However, the collection of radar records used in the present work is original. The specific radar hardware properties and environmental conditions at both sites are outlined in the following.

### *A. Radar Systems*

RiverRad is a pulsed, fully coherent radar developed by the Applied Physics Lab, University of Washington, US (APL-UW). It operates at X-band (9.36 GHz) and provides normalized radar cross sections in co-polarization transmit and receive, in both horizontal and vertical (HH and VV), by alternating records between antennas. This is an active sensor with a nominal transmitted peak power of 6 W that utilizes two parabolic antennas of 60 cm in diameter (one for each polarization) with a pencil beam with an opening of 2.6°. The system was operated in staring mode with a pulse repetition frequency (PRF) of 39.0625 KHz. Twenty of these instantaneous triggers are averaged to form a single data point. The chunk size consists of 512 points, which were used to retrieve the Doppler spectra, which once frequency integrated, yield received power, in what constitutes a record delivered for each range bin. Therefore, the effective dwell time is about 0.262 s for each polarization. The system then alternates between polarization states, resulting in a sampling time step between two consecutive records of the same polarization of about 1.4 s (0.7 Hz). The recording time for each sea state was 2 minutes. The pulse width is 50 ns which yields a nominal range resolution of 7.5 m. However, further details of the pulse shape are not available. A linear amplifier was used to enhance the amplitude of the received signal prior to digitization. Data are delivered in terms of received power, which was then converted into normalized radar cross sections $\sigma_0$ (NRCS). The radar was calibrated using a corner reflector prior to the field campaign (see Catalán et al. (2014) [22] for further details).

Hereon radar is a pulsed, coherent on receive marine radar, developed by the Helmholtz-Zentrum Hereon. It consists of a modified marine radar (GEM Leonardo series) where dedicated electronics were added for radar control, signal amplification as well as digitization, and to steer the antenna in a user-defined direction. It operates at X-band (9.48 GHz) and provides raw backscatter data at a single co-polarization (either HH or VV, depending on the antenna in use), which is then made coherent in post-processing (see Horstmann et al. (2021) [68] for further details). For the present study, a 7.5 ft ($\approx 2.3$ m) wide VV antenna (designed as a slotted wave guide) was used, resulting in a 1.2° azimuthal resolution. The radar transmits with a peak power of 12 kW at a PRF of 2 KHz. The chunk size of 512 pulses was used to compute the Doppler spectra and to obtain the received power and Doppler speed. Therefore, the effective dwell time is about 0.256 s and thus similar to what was used for RiverRad. The use of a single polarization does not require switching between antennas, thus the sampling time step between two consecutive records matches the dwell time (of $\approx$ 0.256 s or 4 Hz). The pulse width at $-3$dB is 70 ns which yields a nominal range resolution of $\approx$ 10.5 m. Similar to RiverRad, the AD converter operated at 20 MHz resulting in a distance of 7.5 m between two consecutive range bins. Thus, the signal is slightly oversampled in range. Like RiverRad, the Hereon radar also uses a linear amplifier. The output of the radar is the digital, complex (I and Q channel) coherent electromagnetic signal for each pulse at every range bin. A total number of 435 range bins are stored yielding a maximum sampled range of about 3.2 km. The recording time for each sea state was 10 minutes. The signal is stored in uncalibrated analog-to-digital units (ADU) of the digitizer and was not converted to NRCS.

In what follows, the analysis focuses on two main radar quantities: a measure of the received backscatter intensities and a measure of the radial surface speeds (along the look direction of the antenna). The first was computed directly from

TABLE I
HARDWARE PARAMETERS FOR THE USED RADARS

| | RiverRad | Hereon radar |
|---|---|---|
| Frequency | 9.36 GHz | 9.48 GHz |
| Polarization | HH / VV | VV |
| Peak power | 6 W | 12 kW |
| Pulse length | 50 ns | 70 ns |
| Pulse repetition frequency | 39.0625 kHz | 2 kHz |
| Antenna type | parabolic ∅ 60 cm | slotted waveguide 7.5' ($\sim$ 2.3 m) |
| Sampling frequency | 20 MHz | 20 MHz |
| Sampled range cells | 111 | 435 |
| nominal resolution | | |
| range | 7.5 m | 10.5 m |
| azimuth | 2.6° | 1.2° |
| range cell spacing | 7.5 m | 7.5 m |

RiverRad as radar NRCS, $\sigma_0$, whereas the Hereon radar was uncalibrated and only provides the RCS. To achieve comparability of the two radars, the Hereon backscatter amplitude was scaled, range corrected and then converted to dB-scale, following Gommenginger et al. [69] . The scaling was adapted so that the data covers the same dB-range as the RiverRad data. For simplicity, the measured backscatter intensity of all data will be referred in the remainder of the manuscript as NRCS or Intensity, without loss of generality. The radial component of the scatterer motion, the Doppler speed, was computed from RiverRad at the frequency of the peak of the Doppler spectrum at each time and range bin by

$$D = \frac{f_p \lambda_0}{2 \sin \theta}, \tag{1}$$

where $D$ stands for Doppler speed, $f_p$ is the peak frequency, $\lambda_0$ is the wavelength of the microwaves, and $\theta$ is the nominal incidence angle. Although Doppler peak separation is usually the preferred method [23], for the sake of comparability, the same Doppler processing was employed to determine $D$ from the Hereon radar data.

The baseline data are thus time series of these quantities at each radar cell in range, which are concatenated to form time-range maps, $I(r,t)$, $D(r,t)$, where $r$ is the ground range in m and $t$ is the elapsed time in s. In what follows, VV polarization is chosen for reporting as it is available in both sensors (compare Tab. I).

### *B. Study Sites and Environmental Data*

The first set of radar records, referred to as DUCK-I, was collected in the northern hemisphere spring (May 2008) using RiverRad, which was deployed over the crest of the dune at the north end of the Field Research Facility of the US Army Corp of Engineers (henceforth FRF), at Duck, NC, USA (see Fig. 1a). The radar was deployed at 36.19106667° N, 75.75238333° W ($x$=54.40, $y$=936.22 in the FRF coordinate system, where the $x$ axis points in the cross-shore direction at 71° from the north), at a height of $z$=10.24 m (NAVD88). For the present data set, only antenna look directions deviating within $\pm 2$ ° from cross-shore have been considered. The second set, referred to as DUCK-II, was collected with the Hereon radar, also deployed at the FRF but during fall (October 2021). It was located at 36.1822972° N, 75.7511785° W ($x$=34.84, $y$=537.37, $\sim 400$ m away from RiverRad location), at $z$=14.72 m (NAVD88). Further details on this specific radar installation are reported by Streßer et al. (2023) [70]. Data were collected with the antenna oriented towards 60° with respect to north ($\sim$ 10° off from cross-shore). For both experiments, environmental data were retrieved from the extensive data collection portal maintained by the FRF. The third set, referred to as SYLT, was collected with the Hereon radar at the Island Sylt during late summer (September 2016), which is a barrier island in the German Bight located in the southern North Sea, at 54.7903°N, 8.2833° E, at an elevation of $z$=28 m. The antenna look direction was cross-shore, 271° with respect to the north. Tidal elevations and 10-m wind speeds were extracted from the operational model BSHcmod [71]. Wave information is available from a directional wave rider buoy (Datawell DWR-MkIII) located in the radar view direction about 1 km off the coast in a

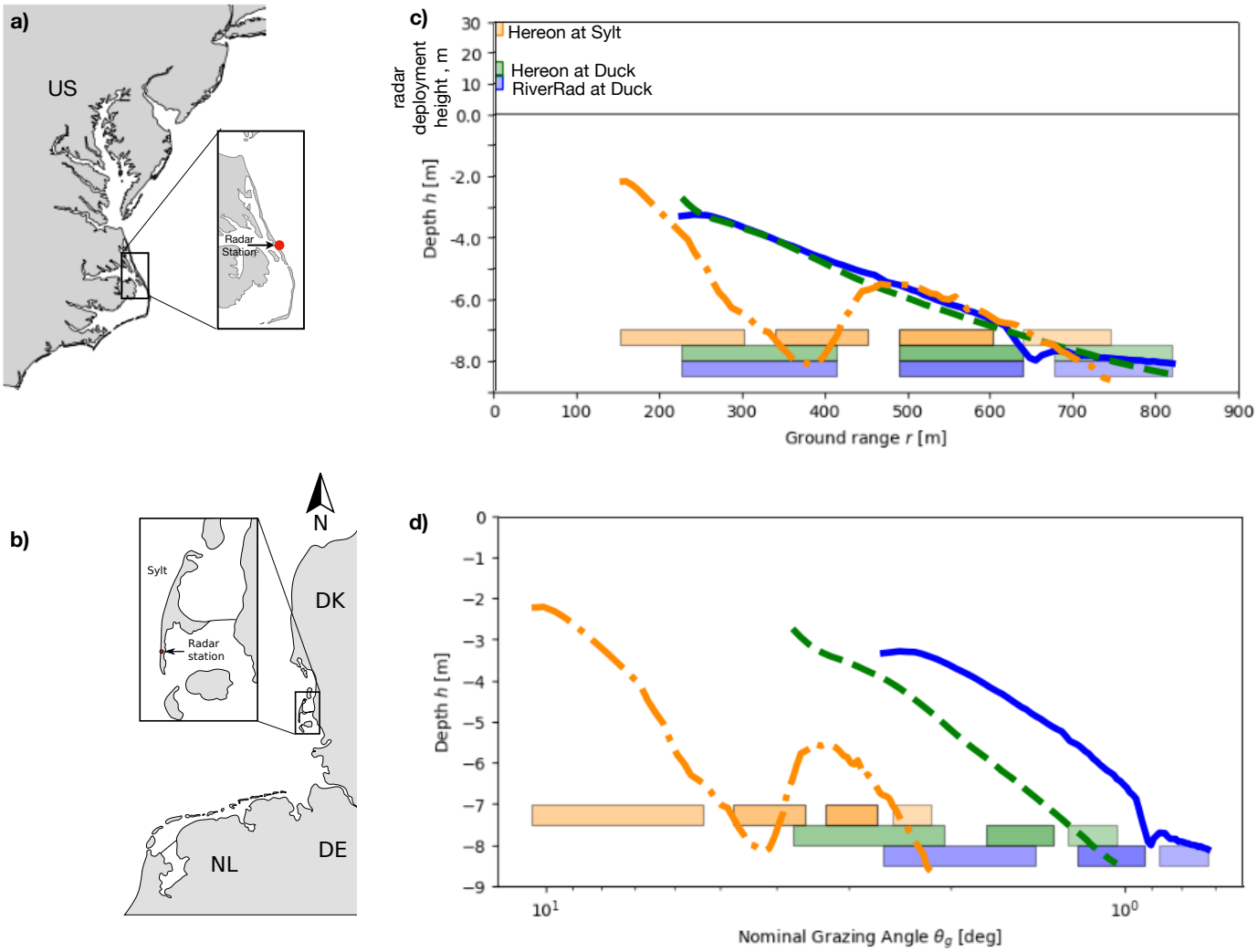


Fig. 1. Radar deployment locations a) DUCK-I and II; b) SYLT. c-d) Representative beach profile transects at all locations expressed as a function of ground range (c) and nominal grazing angle (d). Colored boxes identify the relative locations for the near, mid-range, and far-range analysis performed in this work. SYLT shows in addition boxes at near range to denote a bar trough. In (c), the positive vertical axis is distorted 1:10 to show the relative elevation of the antennas. In all cases, DUCK-I (blue), DUCK-II (green), and SYLT (orange). These colors are retained whenever possible.

water depth of 10 m.

Duck beach is a gently sloping beach, exposed to eastern swells and shorter wind seas from the western Atlantic. Fig. 1c-d shows that despite the 13-year difference between data collections at Duck, the beach profiles are similar. Sylt is also a shallow nearshore, but unlike the conditions at Duck, the foreshore slope is steeper leading to a well-defined trough and a set of two sand bars. As shown in Fig. 1c, this means that data at Duck and Sylt were collected at different water depths at near range ($r < 450$ m), but match well at farther ranges. However, the different antenna elevations lead to mismatching water depths when data are grouped in terms of grazing angle (Fig. 1d).

These differences in terms of range, depth profile, and system elevation, provide a challenging scenario to compare among records, especially if different wave periods are considered, as the wave relative depth encompasses intermediate to shallow water waves. In an attempt to group data, observations at each site have been grouped in terms of ground distance to the antenna, and termed far, mid and near range, respectively (see boxes in Fig. 1c-d). The selection of these regions was based on the observed persistence of breaking, where the far range usually corresponds to the shoaling phase, while the mid and near ranges to the outer and inner breaking. However, these definitions are not persistent among datasets, as the breaking regime will depend on

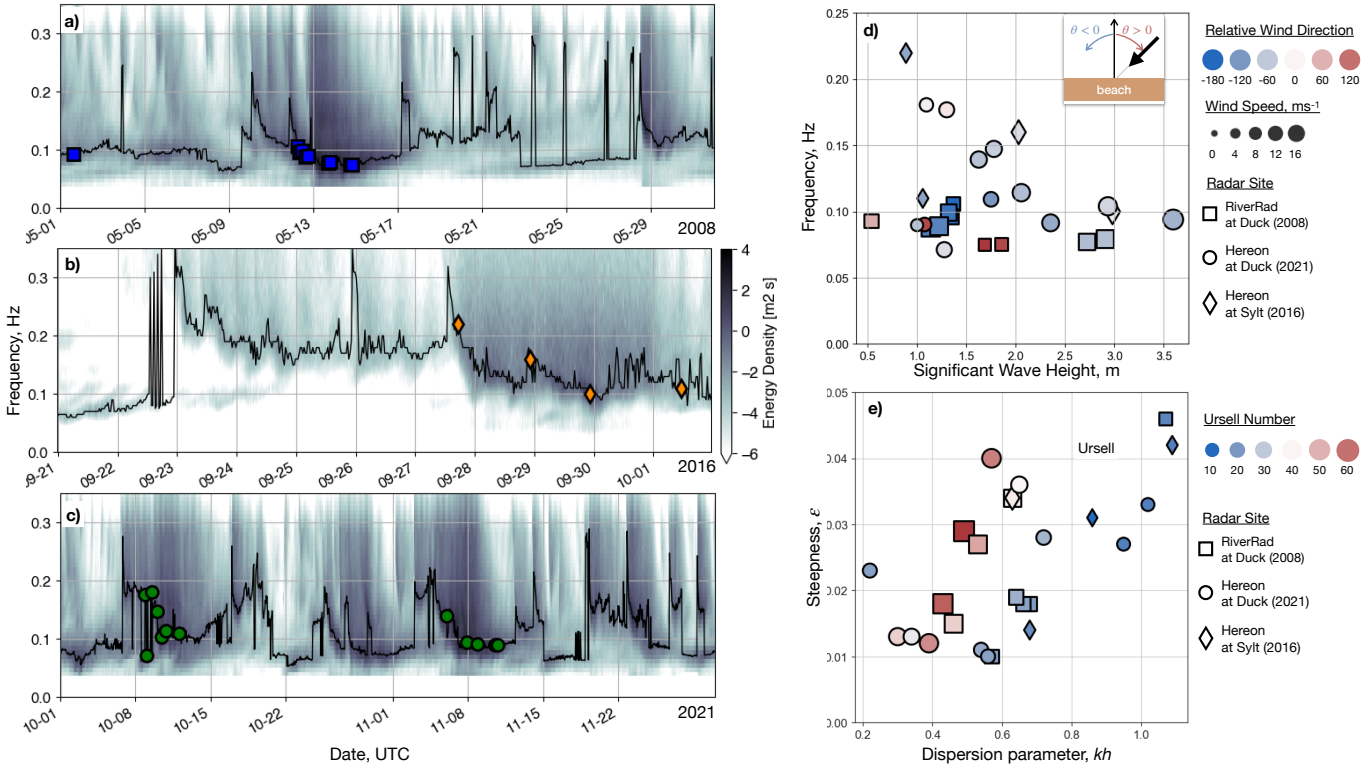


Fig. 2. a-c) Spectrograms of incident wave energy density, in logarithmic scale for all three experiments. The black line follows the peak frequency of the gravity waves, and squares denote all the cases considered in this study (see Table II). a) DUCK-I; b) SYLT; c) DUCK-II. d) Scatter plot showing the distribution of wave height and peak frequency of all data sets. Shapes denote the different sites, colors denote the relative wind direction with respect to shore normal, and sizes denote the absolute wind speeds. Inset schematic exemplifies the wind and wave direction convention. e) Scatter plot showing the distribution of relative depth, steepness and Ursell number (colors).

tidal elevation and wave parameters as well. For this reason, the relative distance nomenclature is retained.

Fig. 2 shows a summary of the wave conditions, which are also listed in Table II, where the peak period $T_p$, significant wave height $H_s$, wave steepness $\epsilon = H_s/L$, 10 minute mean wind speed at 10 m height $U_{10}$ and its direction, relative depth $\mu = kh$, and Ursell number $\mathrm{Ur} = H_s L^2/h^3$ are presented. Note that wind direction is presented using the nautical convention in the Table, whereas Fig. 2 and the remainder of the article use relative directions as deviations from shore normal, positive clockwise. $\epsilon$, $kh$ and $\mathrm{Ur}$ are estimated at the outermost point of analysis (800 m at DUCK-I/DUCK-II and 750 m at SYLT) roughly corresponding to the measurement location of the reference wave data. $L$ is the gravity wave length, $k = 2\pi/L$ its wave number, obtained using the linear dispersion equation, and $h$ the local still water depth. Both DUCK experiments show a mixture of storms with broad seas (shown as darker areas in panels a-c), as well as narrow banded conditions. SYLT data also show broad seas on occasion, though less energetic. The aggregated data show significant wave heights ranging from $H_s$ =0.9 to 3.6 m, and peak periods between $T_p$=5 and 15 s. This range of wave conditions leads to a spread in other relevant wave parameters. Fig. 2d highlights the distribution of the data in terms of wave height, peak period (plot axes), as well as wind speed and direction (sizes and colors). Similarly, Fig. 2e shows the distribution in terms of relative depth, steepness, and Ursell number. It can be seen that data are well scattered, with the exception of certain concentrations towards periods of about 10-15 s. Hence the aggregated dataset encompasses two different radar systems at the same beach, and two beaches observed by one of the radars. Environmental conditions range from shallow water to intermediate water waves (based on $\mu = 0.22 - 1.09$), wave steepness range from $\epsilon \approx 0.01 - 0.05$, and Ursell numbers up to 62. Therefore, linear and non-linear waves are present, which can be relevant in terms of the range of actual

free surface slopes illuminated by the radar.

### C. Data Analysis

*Identification of Breaking Waves:* For the analysis, it is relevant to distinguish between breaking and non–breaking waves, both to isolate underlying physical processes as well as the associated imaging mechanism. This is a challenging task in microwave remote sensing owing to the apparent lack of a clear signature from breaking waves (Streßer et al. (2021) [23] and Catalán et al. (2011) [28] offer broad reviews on the detection of breaking waves). For the purpose of this work, three different techniques were compared using data from DUCK-I as a first step in the analysis. The chosen criterion is based on the ratio of phase speed to crest orbital speed as introduced by Barthelemy et al. (2018) [1]. The phase speed of the imaged waves is unknown and herein approximated by the shallow water phase speed $c = \sqrt{gh}$. Waves are classified as breaking when the horizontal component of the wave orbital speed (assumed to correspond to the Doppler speed measured by the radar) exceeds 0.85 times the shallow water phase speed. The criterion proved to be more robust and conservative than two other criteria (see Supplementary Material for details). However, it should be noted that the criterion is based on assumptions that might not always hold. False classifications are to be expected for breakers that are shorter than the dominant waves hence travel slower, and non-linear waves travelling faster than the shallow water phase speed [72]. Furthermore, the criterion relies on the approximation that the measured Doppler speed corresponds to the horizontal component of the wave orbital velocity. Despite these possible shortcomings, it is expected that reasonable discrimination can be achieved consistently for most of the data.

*Extracting radar-facing slopes:* For the analysis, the leading parameter will be the maximum

TABLE II

ENVIRONMENTAL DATA SUMMARY. PEAK PERIOD $T_p$, SIGNIFICANT WAVE HEIGHT $H_s$, WAVE STEEPNESS $\epsilon$, WIND SPEED AT 10 M HEIGHT $U_{10}$ AND ITS TRUE NORTH DIRECTION IN PARENTHESES, RELATIVE DEPTH $\mu$, AND URSELL NUMBER Ur. CASES HIGHLIGHTED IN ITALIC FONT ARE USED IN FIGS. 5-6.

| Casename | $T_p$ [s] | $H_s$ [m] | $\epsilon$ [-] | $U_{10}$ (dir) [ms$^{-1}$] ([°TN]) | $\mu$ [-] | Ur [-] |
|---|---|---|---|---|---|---|
| DUCK-I, 16846 | 10 | 0.9 | 0.010 | 7 (140) | 0.57 | 14 |
| DUCK-I, 22548 | 9 | 1.4 | 0.018 | 8 (264) | 0.70 | 14 |
| DUCK-I, 22348 | 8 | 1.9 | 0.026 | 17 (153) | 0.75 | 17 |
| DUCK-I, 22608 | 10 | 1.4 | 0.018 | 9 (265) | 0.66 | 15 |
| DUCK-I, 22686 | 10 | 1.5 | 0.019 | 11 (279) | 0.64 | 18 |
| DUCK-I, 22806 | 6 | 2.3 | 0.046 | 15 (292) | 1.07 | 9 |
| DUCK-I, 22888 | 11 | 3.1 | 0.034 | 17 (300) | 0.63 | 34 |
| ***DUCK-I, 23606*** | *12* | *2.8* | *0.027* | *13 ( 17)* | *0.53* | *45* |
| DUCK-I, 23546 | 13 | 3.2 | 0.029 | 14 ( 13) | 0.49 | 62 |
| DUCK-I, 23582 | 12 | 2.9 | 0.030 | 13 ( 55) | 0.43 | 59 |
| DUCK-I, 24261 | 13 | 1.8 | 0.018 | 5 (230) | 0.43 | 56 |
| ***DUCK-I, 24266*** | *13* | *1.8* | *0.015* | *5 (230)* | *0.46* | *39* |
| DUCK-II, case6 | 7 | 1.8 | 0.033 | 10 ( 33) | 1.02 | 8 |
| DUCK-II, case7 | 10 | 2.9 | 0.036 | 15 ( 40) | 0.65 | 32 |
| DUCK-II, case8 | 9 | 2.0 | 0.028 | 13 ( 15) | 0.72 | 19 |
| DUCK-II, case9 | 9 | 1.7 | 0.023 | 7 (329) | 0.22 | 15 |
| DUCK-II, case10 | 15 | 1.3 | 0.013 | 8 ( 29) | 0.30 | 39 |
| DUCK-II, case11 | 14 | 1.3 | 0.013 | 8 ( 47) | 0.34 | 29 |
| DUCK-II, case12 | 13 | 1.1 | 0.012 | 5 ( 66) | 0.39 | 18 |
| DUCK-II, case13 | 7 | 1.6 | 0.027 | 11 ( 19) | 0.95 | 8 |
| DUCK-II, case14 | 11 | 3.6 | 0.040 | 19 ( 1) | 0.57 | 51 |
| DUCK-II, case15 | 13 | 1.1 | 0.012 | 5 ( 66) | 0.39 | 49 |
| DUCK-II, case16 | 11 | 1.1 | 0.011 | 6 (236) | 0.54 | 17 |
| DUCK-II, case17 | 11 | 1.0 | 0.010 | 3 ( 19) | 0.56 | 15 |
| SYLT, case2 | 6 | 2.0 | 0.042 | 12 (246) | 1.09 | 8 |
| ***SYLT, case3*** | *10* | *3.0* | *0.034* | *14 (265)* | *0.63* | *35* |
| ***SYLT, case4*** | *9* | *1.1* | *0.014* | *5 (184)* | *0.68* | *11* |
| SYLT, case5 | 5 | 0.9 | 0.031 | 6 (189) | 0.86 | 3 |

NRCS at any given time step $t = t^*$, and denoted as $I_{\text{peak}}$. The along range location of the NRCS maximum is stored, $r^*$. The assumption is that the most energetic scatterers traveling with the gravity wave are located at the radar facing side [23]. Under the composite surface model, they correspond to the steepest part of the wave, or the wave roller during breaking. Individual data points are obtained from the range axis for each time step. For the peak extraction, the zero-crossing technique is employed after shifting the data for all points in the section over time to the zero mean. The concurrent value for the Doppler speed, $D(r^*, t^*)$, is retrieved at the same position as the intensity peak.

*Conditional histograms:* A statistical evaluation of the cases indicated in Table II is obtained by comparing conditional Doppler speed—Intensity histograms for each one of them. The data for the histogram includes the entire measurement period for each case but due to the heterogeneous nature of shoaling, the spatial extent was limited by separating into range sections as shown in Fig. 1. The interpretation of the histograms was simplified by limiting the analysis to data points extracted at each intensity peaks within the regions of interest (cf. Fig. 1c-d). Distinguishing between breaking and non–breaking waves leads to two groups per region per case. From them, the bivariate distribution of the $I_{\text{peak}}$ and its concurrent Doppler speed is constructed. However, to simplify the presentation of the results, the bivariate histograms show only the regions where the number of occurrences exceeds a given threshold. The threshold for non–breaking waves is 15% of the peak occurrence while it is 1% for breaking waves. The different thresholds aim to find the optimal compromise between robustness and including as many cases as possible. For breaking waves the contours are still robust even for this very low threshold. To achieve smooth contour lines, the histograms were smoothed by applying a Gaussian filter with a unit standard deviation. The center of mass of the histogram is indicated by markers, and it is used as a representative value of the data. An example from the data extraction to the retrieval of the contour lines is illustrated in the Supplementary Material. Similar histograms without scaling were analyzed by Farquharson et al. [66] and [23]. Both used all data, not just wave fronts as done herein, for a single wave condition but varying surf zone locations.

*Scaling:* Doppler speeds are scaled by values representative of the observed physics for comparison among data sets (e.g. when comparing histograms). Breaking waves are normalized by the shallow water phase speed, $c = \sqrt{gh}$, since the Doppler return is dominated by the speed of the roller [73]. This value is expected to be a lower bound for surf zone waves [52], [72]. In contrast to that, the Doppler speed of non–breaking waves is expected to be characterized by the projection of the orbital velocity vector along the radar look direction [74]. However, for low grazing the vertical component can be neglected and for the present cases, the radar azimuthal directions have been constrained to small deviations. Non–breaking waves are therefore scaled by the maximum value of the horizontal component of the orbital velocity, expected to occur at the wave crest, and approximated by linear theory as

$$u_{\max} = \frac{\pi H_{\text{eff.}} \cosh\left(k(h + H_{\text{eff.}}/2)\right)}{T_p \sinh(kh)}, \qquad (2)$$

where $H_{\text{eff.}}$ denotes the effective wave height, which is assumed to be $H_s$ in sufficiently deep water and $0.45\ h$ otherwise, which is well in the range of saturated wave heights typically observed in the inner surf zone of natural beaches [75]. The effect of surface currents and drift has been omitted to provide a manageable comparison value.

The remaining variables are the wavenumber $k$ and the peak period $T_p$. A comparison of phase speed scaling and orbital velocity scaling for non–breaking waves is contained in the Supplementary Material.

*Wave tracks:* The averaging introduced in constructing the histograms restricts the understanding of the evolution of the backscattering parameters as the waves shoal. For that purpose, a wave tracking algorithm was applied to extract the evolution of single waves [76]. The algorithm is a slightly modified version of the edge detection by Grompone von Gioi and Randall (2017) [77]. Edges are first defined according to the Canny algorithm, where all image points whose gradient exceeds a given threshold are selected. Then they are chained and also extended to gradients exceeding a second lower threshold. An additional application of the Devernay procedure ensures that the edges are straightened. This is accomplished by defining the edges on a grid with higher resolution and hence allowing edges to

traverse pixels. For the present purposes, it was of interest to follow the position of the NRCS peak, which was assumed to be located in the vicinity of the detected edge. The speed is estimated directly as the slope of the time-space evolution of the intensity peak. An example of the automatically extracted wave tracks is displayed in the Supplementary Material. Finally, data surrounding (in space) the tracking of the peak are retrieved to obtain the along-range shape of the NRCS and Doppler speed to allow for observing its space and time evolution as the waves shoal.

## III. Results

### A. Conditional Doppler speed-NRCS Statistics

Fig. 3 shows sample results (additional plots are presented in the Supplementary Material). Here, the distribution of NRCS and normalized Doppler speeds is limited to the radar facing slopes (c.f. Sec. II-C) for non–breaking waves at mid range for the three experiments are presented. All panels share the same data, and the difference among them is the highlighting of data corresponding to the criterion shown for each panel.

Most of the data span a wide range of intensities (as seen by the vertical spread), with an upper limit at about $I \approx -30$ dB. Normalized Doppler speeds also show a wide range, from negative values (moving away from the antenna) to values that can reach up to three times the theoretical maximum orbital speed of the dominant waves, though the bulk of the data is well within 0-2 times $u_{\max}$. Most of the contours belong to single connected regions whose centroids tend to concentrate around a narrow range of normalized Doppler speeds, although with some larger variability in terms of NRCS. The contours reflect both the spread due to the variability of waves within each sea state and the transformation the waves encounter during their passage through the observed range section. For example, assuming for a moment that the bacskcattering is due to composite surface theory, contours that are oriented mostly vertical (for instance, the blue contour in panel Fig. 3k ) could be interpreted as arising from non–breaking waves with varying radar facing slopes. An horizontal contour (e.g. orange contour in Fig. 3e) would indicate waves of nearly constant slope, but varying Doppler speeds. Oblique contours would suggest wave shoaling, as waves evolve from lower steepness and lower speeds to higher steepness and higher speeds. These wave kinematic processes are captured by the radar, as will be shown by single wave tracks in Sec. III-B starting from low $D/u_{\max}$ and low $I$ (the lower left in the figures) and transitioning towards high $D/u_{\max}$ and high $I$ (the upper right). Hence narrow elongated contours witness of a distinct shoaling signature while rounder contours are strongly affected by the variability between waves at each range.

The aggregation of data allows us to compare the validity of the assumption, when data are grouped by different criteria. The top row shows the distinction between experiments highlighted in color (the coloring is retained for the remainder of the manuscript). Data collected during the DUCK-I campaing shows similar spread of intensity as that of DUCK-II, but Doppler speeds seem to be lower. In contrast, SYLT data has intensities in the upper range of values, and Doppler speeds that are as fast as DUCK-I.

The second row of Fig. 3 demonstrates how the Doppler speeds experience a transition depending on the wind direction. The criteria for classifying the datasets was

$$U_{10}\cos(\Delta\phi)\begin{cases} > 4\ \mathrm{ms}^{-1} & \text{Offshore wind} \\ \in\ [-2;2]\mathrm{ms}^{-1} & \text{Little wind} \\ < -4\ \mathrm{ms}^{-1} & \text{Onshore wind,} \end{cases} \tag{3}$$

where $\Delta\phi$ denotes the angle between wind direction and radar look direction. The definition ignores cases of intermediate wind speeds for all directions. The overall effect of wind leads to a shift in the Doppler speeds which transitions from low Doppler speeds when wind is blowing offshore, to larger Doppler speeds when wind is blowing onshore. While this could be interpreted as the Doppler speed also containing information about the wind drift, attempts to correct using the standard value of 3% [66], [78] did not improve the results significantly. The other two rows show grouping when data are below (third row) or above (bottom row) prescribed thresholds for wave steepness, relative depth and Ursell number. The nominal values of the parameter used for discriminating are estimated using the offshore wave conditions, as there are no wave height measurements available throughout either surf zone. A clear distinction between cases is not apparent.

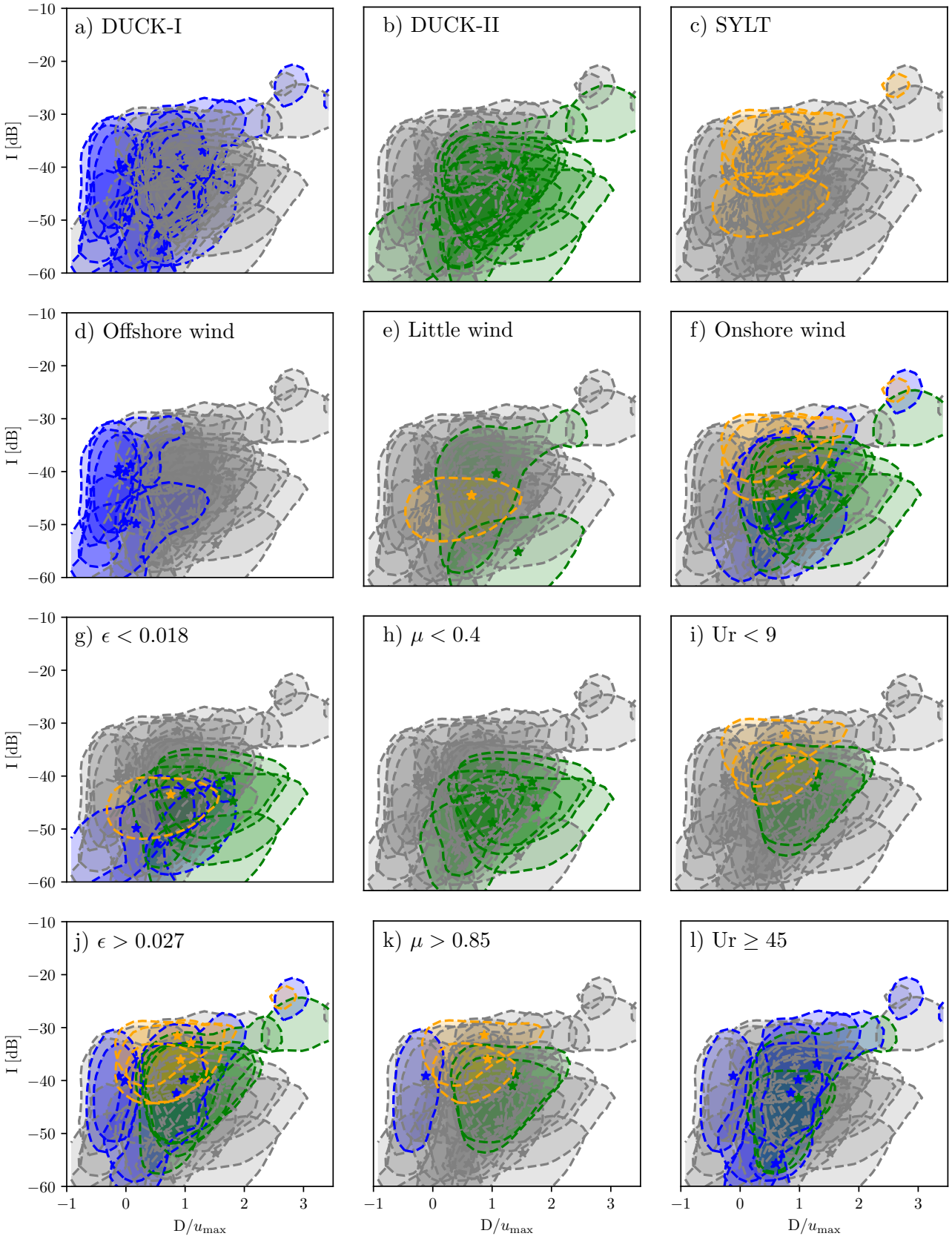


Fig. 3. Bivariate histograms of normalized Doppler speed and NRCS for the aggregate of all datasets. All panels show the same data with highlighted data fulfilling the following criteria: a) SYLT; b) DUCK-I; c) DUCK-II; Influence of wind (d,e,f), wave steepness $\epsilon$ (g,j), relative depth $kh$ (h,k) and Ursell number; (i,l); Each sea state is represented by a contour line.

A closer look at the different panels reveals that the wave kinematics depend on the combinations of wave, wind and beach parameters. To fully understand the figure it requires to identify distinct contours in different panels:

1) The cases of offshore wind contain two examples with high initial steepness ($\epsilon > 0.027$, panel j) and one with low steepness ($\epsilon < 0.018$, panel g). While the intensity grows by a comparable amount in all cases, the normalized Doppler speed only increases considerably for the case with low steepness (offshore wind and high steepness: $[-0.7, 0.2]$, offshore wind and low steepness: $[-1.0, 1.2]$).
2) In comparison to offshore wind, the cases of onshore wind generally encompass a wider range of normalized Doppler speed values (offshore wind: $[-1.0, 1.2]$, onshore wind: $[-0.3; 3.5]$).
3) When distinguishing according to the steepness, we observe that in the histograms of high initial steepness (panel j) the shapes are dominated by an increase of the NRCS while for low initial steepness (panel g) the increase in $D/u_{\max}$ is dominating. It should be noted that the low steepness cases (panel g) are also cases of low relative depth ($\mu < 0.4$, panel h) and that the available data does not contain examples of steep shallow water waves.
4) According to theory [79], cases of low Ursell number (Ur) do not fall under the shallow water regime. The presented analysis illustrates this effect in panels i and k: Low Ursell numbers correspond to large relative depth ($\mu$). It should also be noted that the low Ursell number cases were all subject to onshore wind (panel f) and initial high steepness (panel j). Cases of high steepness that do not fall under the onshore wind regime have less increase in the Doppler speed values. Therefore it is inferred that for the low Ursell number cases, it is the onshore wind that causes the increase in Doppler speed values up to 2 $u_{\max}$.
5) The most uniform shape of contours was found for cases of high Ursell number (panel l). The contours are elongated and extend over a substantial range of NRCS. The relation in the growth rates of NRCS and $D/u_{\max}$ remains constant up to a certain NRCS level where the intensity growth stops and only the Doppler speed increases. Assuming that the NRCS reflects the local wave steepness, the observations for high Ursell numbers confirm previous findings: In the shallow water regime, the acceleration of the water balances the local steepening. (Peregrine 1983, [79]). The wind appears to influence the inclination of the growth rate relationship (as evidenced by the obliqueness of the contours). Five out of the seven highlighted cases have shared characteristics and occur during low wind conditions. The onshore wind case (indicated by the large blue contour in panel f) is slanted towards higher Doppler speed values, while the leftmost contour, an offshore wind case, is tilted and shifted towards lower Doppler speed values.

Further analysis of the wind influence, including near and far range, will be presented in Sec. IV. Additional examples of panels g–l for other range windows are available in the Supplementary Material. Despite a clear shifting of the histograms along the intensity axis, the behavior described above still holds. As the nominal ground range to the antenna decreases (or the grazing angle increases), the NRCS increases, which is in line with Bragg and composite surface theory.

Similar histograms but for breaking waves are shown in Fig. 4, where individual cases are highlighted. Unlike the previous analysis, signatures of breaking waves are expected to be independent on range and depth and hence considered in unison. The different range sections are distinguished by the line type (far range: dotted, mid range: dashed, near range solid). Data show less difference in normalized Doppler speed among data sets, where typical values are constrained near $\frac{D}{\sqrt{gh}} \approx 1.0-1.5$. Though the lower normalized values are constrained by definition, there is an upper limit of speeds that lies around 1.6. This value is consistent observed deviations from linear theory phase speeds due to wave non-linearity in laboratory experiments [72]. For breaking waves, DUCK-I and II data show distinct NRCS values across experiments, with the lower grazing angle DUCK-II data yielding lower values, that compare well with the farthest (hence lower grazing shown in dashed turquoise in Fig 4a) DUCK-I case. However, two DUCK-II cases at

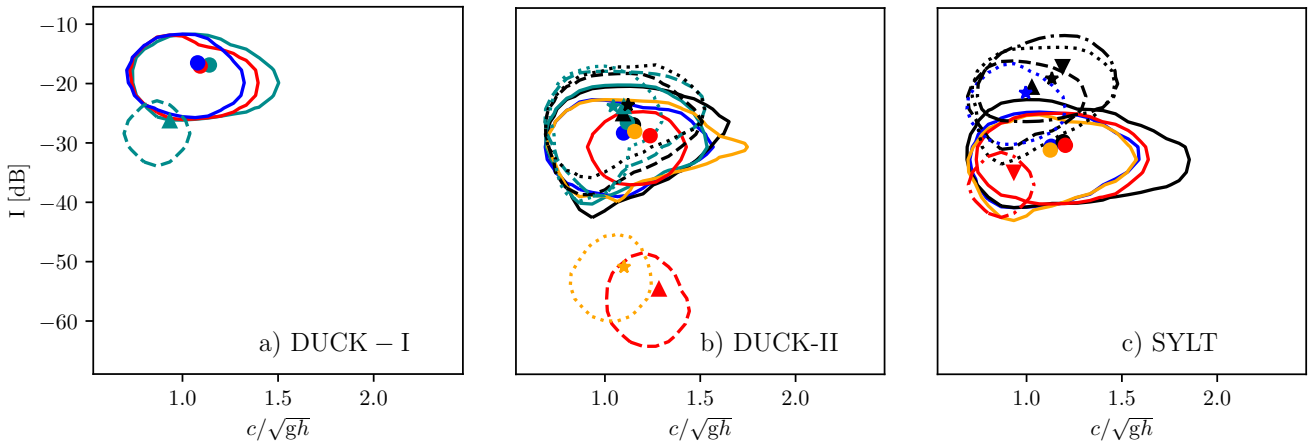


Fig. 4. Bivariate histograms of normalized Doppler speed and NRCS of breaking waves estimated for each case. Colors and line types denote different cases and the relative locations. a) DUCK-I; b) DUCK-II; c) SYLT. The linestyle and the markers differ according to the chosen range section. For DUCK-I and DUCK-II solid lines and circles denote the near range, dashed line and triangles mark the mid range and dotted lines and stars represent the far range. For SYLT solid lines and circles denote the first bar, dashed line and triangles mark the trough and dotted lines and stars mark the second bar and dashed dotted lines and a reversed triangle represent the far range. The cases are sorted from low to high steepness and the respective color for each one is provided. a) 24266 (red), 23606 (turquoise), 22686 (blue) b) case16 (yellow), case17 (red), case7 (turquoise), case6 (blue), case14 (black) c) case4 (yellow), case5 (red), case2 (blue), case3 (black).

mid and far range show outlier behavior. In turn, SYLT data match well either DUCK data in terms of NRCS range. However, the dependency on grazing angle is reversed, with lower grazing data yielding larger NRCS. A possible reason will be presented in the discussion (Section IV). Both NRCS or normalized Doppler speeds appear to be independent of sea state or environmental conditions.

### *B. Wave Evolution*

The wave tracking and wave breaking detection procedures are used to follow individual waves as they progress shoreward. Figs 5-6 show the results for the four cases highlighted in Table II, where a single wave of each set has been followed in detail. The upper left panel shows the along-wave profile of the NRCS in orange, and its corresponding Doppler speed in blue. The dots correspond to the intensity peak and its associated Doppler speed value. The red marks denote waves that have been identified as breaking, based on the criterion $D > 0.85\sqrt{gh}$, as explained in Section II-C. These are shown on the bottom panel as solid line (wave track-derived speed), dashed line (reference shallow water phase speed), and the depth profile in gray. The right panel shows the Doppler speed-NRCS time history of the intensity peaks (henceforth termed D-I tracks), where Doppler speeds are now presented without normalization. Since data were sampled at every time step, the relative distance between points is a function of its phase speed. The selection of the highlighted wave was arbitrary, but its D-I track does not depart from other waves in the set, shown in light gray, which is indicative of similar behavior among them. These tracks should be followed from the dot symbols, that indicate the offshore-most data point.

Most waves and their D-I tracks show qualitatively the same behavior. They begin at a low intensity level and low Doppler speeds and they traverse upward in the D-I space, meaning an increase in NRCS, but with varying rates of change in Doppler speed. The larger the speed change, the more horizontal the track becomes. Most of the waves show an change in NRCS at first, without significant Doppler speed change (i.e., the track is virtually vertical. This is followed by a simultaneous change in NRCS and Doppler speeds (oblique lines) to be followed by smaller change in NRCS and abrupt changes in Doppler speed, where the track becomes nearly horizontal. Eventually, they reach breaking (here denoted by red triangles) which is typically characterized by the largest NRCS and Doppler speeds. Notably, breaking NRCS values are typically in the approximate range of NRCS [−30 dB; −20 dB], consistent with the histogram analysis

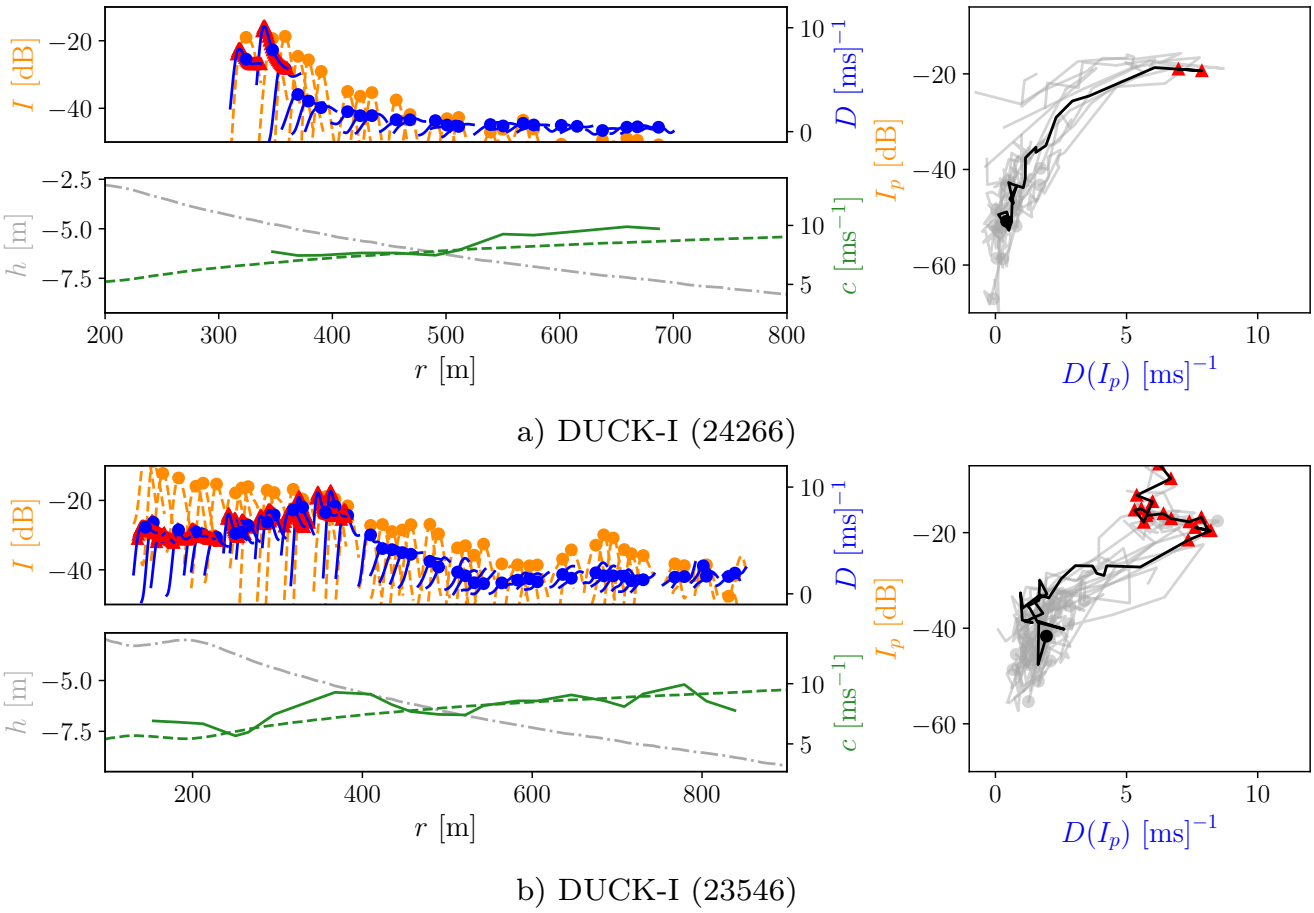


Fig. 5. Wave characteristics along the track of the intensity peak from DUCK-I for two different sea states. Panels (a-c): case 24266 ($H_s = 1.8$m, $\epsilon = 0.018$); Panels (d-f): case 23546 ($H_s = 3.2$m, $\epsilon = 0.030$). (a,d) The evolution of intensity (orange) and Doppler speed (blue); values with largest intensity peak marked by dots; (b,e) Water depth (gray), measured crest velocity as solid line and $c = \sqrt{gh}$ as dashed line. (c,f) Doppler speed–Intensity paths based on the values at peak intensity. Gray lines indicate all waves present in the record, with the highlighted black tracks corresponding to the wave shown in panels (a,d). In all plots breaking instances are indicated by red triangles.

and the values reported in [22], [66]. In some cases, the track reverses horizontally, meaning a Doppler speed decrease while still breaking, e.g. Fig. 5b). Fig. 5a) corresponds to low steepness waves that show a weak change in Doppler speed at first which then augments rapidly. Another case of low wave steepness with a similar behavior is shown in Fig. 6a). In contrast to the former case, these waves are characterized by a higher NRCS at the beginning of the track that does not vary significantly until the waves speed up. Another example is provided in Fig. 6b). Here the wave breaks twice, first over the offshore bar, after which it stops breaking and intensities and Doppler speeds decay as the wave deshoals over the bar trough, to resume breaking near the shoreface at short ranges. Remarkably, the NRCS of this breaking event is among the lowest of the set.

The behavior of these data in the D-I space is well correlated with the distribution observed in the histograms. Histograms with vertically oriented contours can be interpreted as arising from mostly non–breaking waves that are shoaling, whereas oblique contours suggest waves that transition towards wave breaking, speeding up and increasing its NRCS. The relative insensitivity to environmental conditions to other wave parameters is the result of the narrow range of high NRCS and large Doppler speeds identified in breaking waves.

However, these figures also show that NRCS and Doppler speeds can be large, even for instances when the wave has not been identified as a breaking wave, which indicates the difficulty of using either metric as sole wave breaking indicator. Additionally,

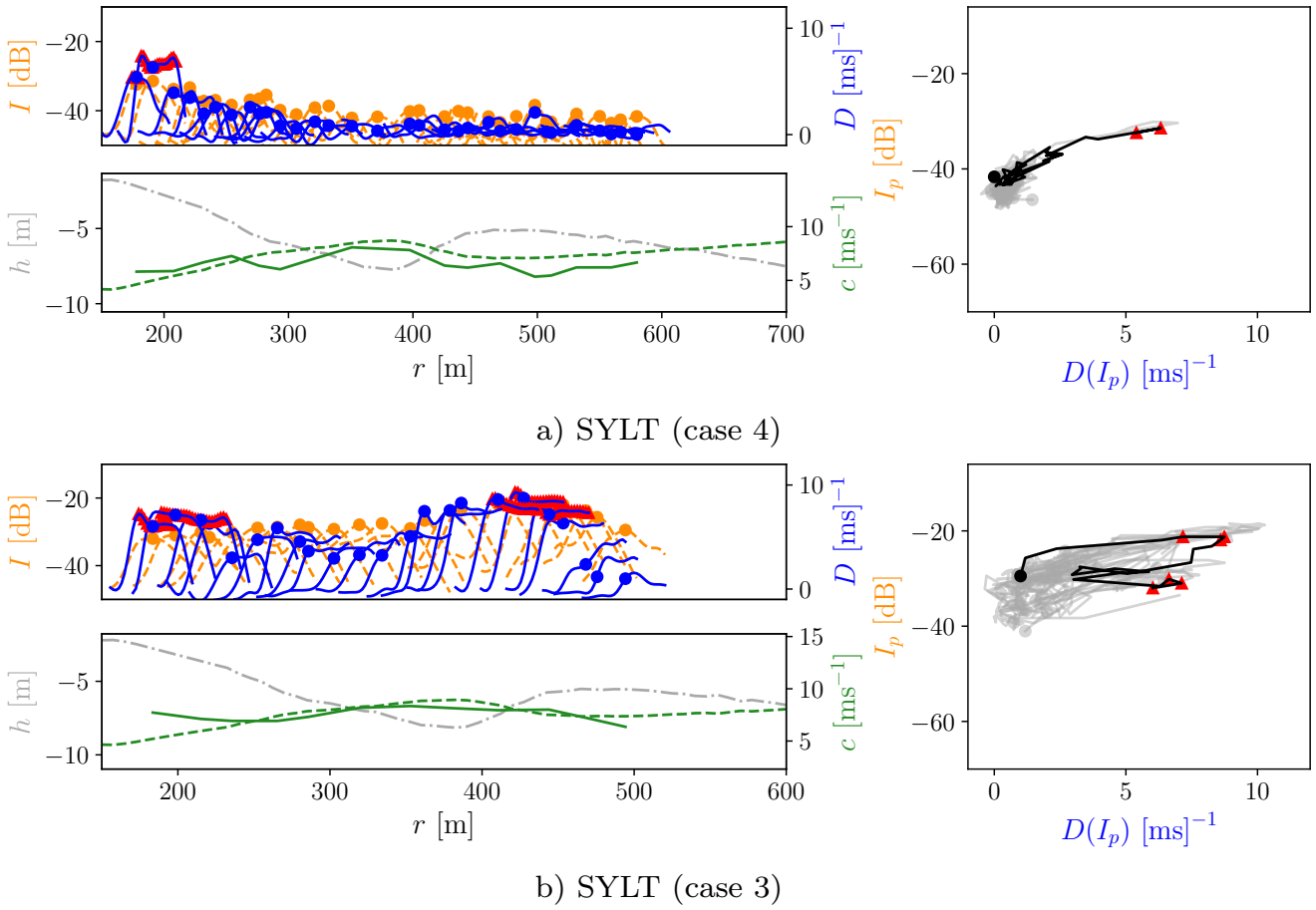


Fig. 6. Same as Fig. 5 for wave characteristics along the track of the intensity peak from SYLT for two different sea states. Panels (a-c): case4 ($H_s = 2.0$m, $\epsilon = 0.014$) in (a-c); Panels (d-f): case3 ($H_s = 3.0$m, $\epsilon = 0.034$).

the peak NRCS rarely corresponds to the position of the Doppler speed peak. In some cases, the Doppler speed peak is located seaward of NRCS peak (compare orange and blue lines, as well as their maxima). This behaviour typically occurs during shoaling. When waves break, the relative distance between both peaks is reduced, and even reduced to zero. This is analyzed in detail below.

## IV. Discussion

In what follows the obtained results shall be discussed in light of existing knowledge on radar backscatter theory. Typically the total backscatter is explained as a composition of Bragg and non-Bragg components (e.g. [61]). For the former, the Composite Surface Theory (CST) is expected to explain the backscattering conceptually, where Bragg waves of a given variance are considered uniformly distributed over the ocean surface and the longer gravity waves modulate their returns by means of tilt and hydrodynamic modulations. Non-Bragg effects involve nonlinear, mostly non-polarized effects often associated to steep and breaking waves at different scales (dominant breakers at scale of the peak wave length, small whitecaps at meter-scales, and microbreakers at decimeter-scales and smaller). Their relative contribution depends on weather conditions and local hydrodynamic factors such as currents and depth. Previous studies have focused on spatiotemporal averaging (among others e.g. [20], [80] and [36] for spatial averages for scatterometers). These averages can be compared to the moments of the histograms that reveal an overall trend in the data but fail in displaying the individual wave dynamics during their evolution. In the following, we discuss effects specific to the

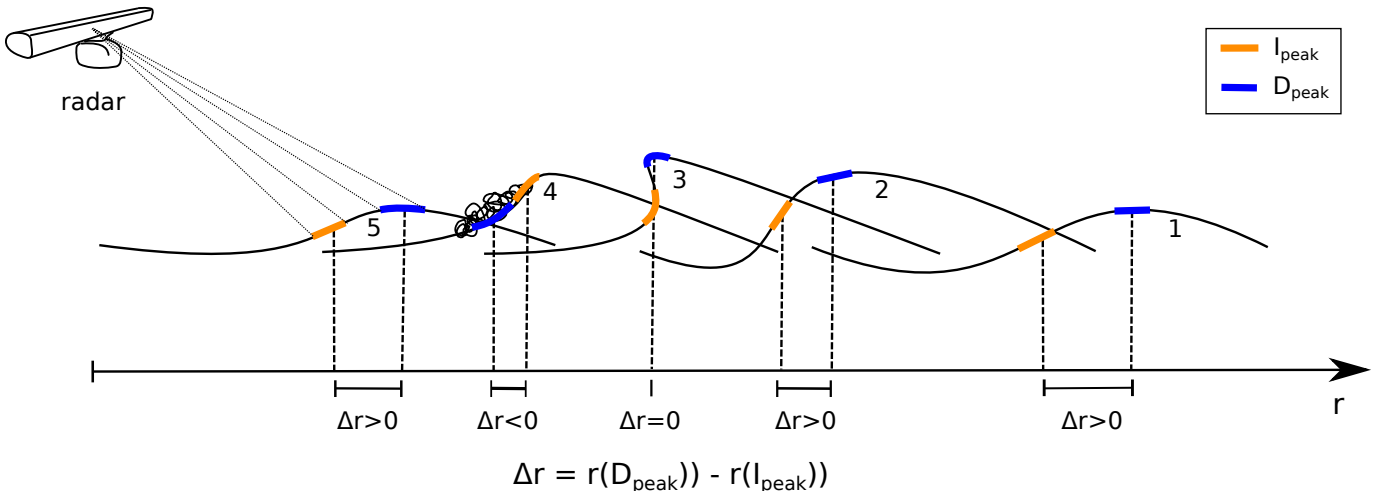


Fig. 7. Sketch of the wave evolution showing steepening and breaking wave stages, as observed by a coherent radar. The along wave locations of yielding maximum Doppler speed ($D$) and NRCS ($I$) are marked. Under low grazing conditions, part of the maximum intensity area is not visible at all times.

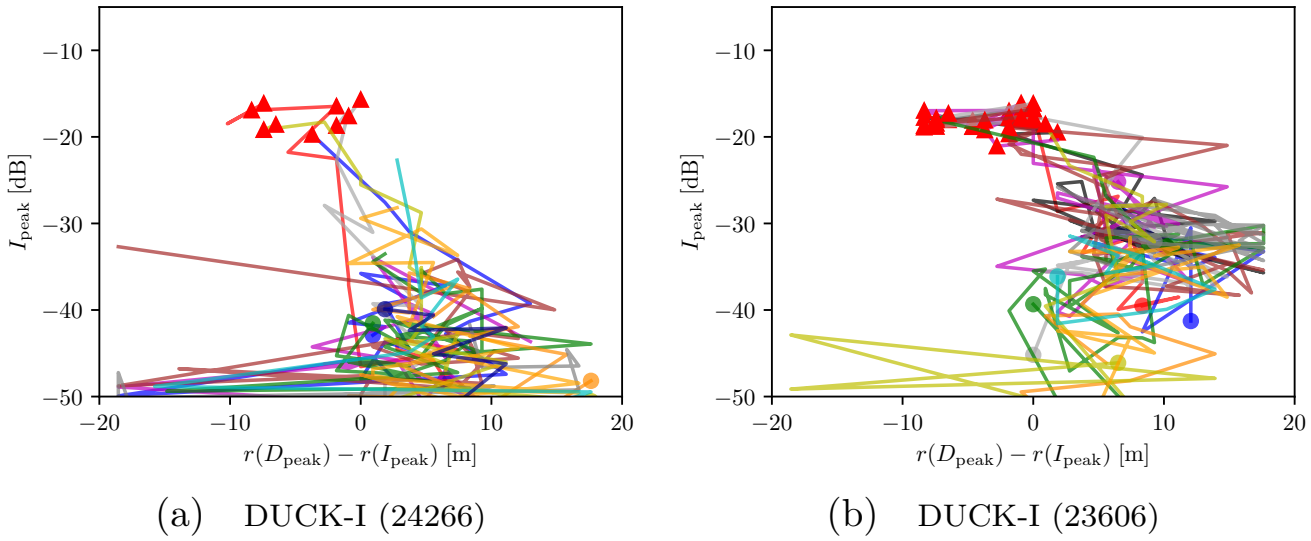


Fig. 8. The evolution of shifts between Doppler speed peak and intensity peak along wave tracks. The starting point of the wave track is marked by a dot, breaking is marked by red triangles.

waves' evolution.

Let us begin by neglecting non-Bragg effects and assume that backscattering arises solely from first order hydrodynamics. The schematic presented in Fig. 7 is used to guide the analysis, where the term "waves" denotes the long gravity waves. For the range of periods considered in this study ($T_p > 9$ s, with a few exceptions), typical wavelengths at water depths of $h \approx$ 7 m are in the range $L > 70$ m, that is, more than $\sim 10$ radar resolution cells. Hence, for purely sinusoidal waves, 2-3 radar cells would cover the front face of the wave. The spread and normalized magnitude of the Doppler speeds is consistent with a change in the scatterers and their relative position with respect to the long wave, as illustrated in Fig. 7. When waves are non–breaking (stage 1, 2 and 5), the location of the maximum orbital velocity is expected to occur at the wave crest, which would yield the maximum Doppler speed. However, the maximum NRCS will be located in front of the crest where the local incidence angle is smaller. This is true for HH, as the Bragg scattering coefficient $|g_H|^2$ is monotonic with incidence angle. For $VV$ the Bragg scattering coefficient $|g_V|^2$ is

not monotonic and peaks around $\theta_i \approx 60°$ [81]. Hence the NRCS maximum will be where the local incidence angle fulfills $|\theta_i - 60°|$ to be minimal. Occurrences of $\theta_l < 60°$ are restricted to very steep waves under low grazing conditions. As a result of this dependency on local incidence angle, the distance between the NRCS peak and the maximum Doppler speed will transition along the wave track. This is illustrated for stages 1, 2, 3 and 5 in Fig. 7, and shown from the data in Fig. 8. For non–breaking waves, the Doppler speed peak trails the location of the maximum NRCS by several meters, with typical values of order 10 m. As can be seen from Fig. 5 and 6, the Doppler speeds in the histograms are biased towards values below the Doppler speed peak due to the estimation at the maximum NRCS. As the wave propagates shoreward, the difference between the peak locations is reduced gradually until both are nearly collocated along the range axis, although the dominant contribution to the Doppler speed and intensity values stem from scatterers at different sections of the surface (e.g. Stage 3). Once the wave breaks, the scattering model departs from CST. It has been typically assumed to be the result of scattering from a very rough surface, the wave roller, that leads to high NRCS, large Doppler speeds, and a broad Doppler spectrum because the scatterers now travel with the wave phase-locked with it. The examples in Fig. 5 and 6 suggest that for breaking waves, within the extent of a resolution cell, the Doppler speed peak coincides, or even leads the NRCS peak. The observed shift between Doppler speed peak and intensity peak is expected but, to our knowledge, it has not been documented in field observations before.

Up to this point, some of the results can be explained in terms of CST and the difference between breaking and non–breaking waves, therefore explainable in terms of gravity wave kinematics. However, other aspects should be considered. The role of wind on the scattering characteristics has been long recognized to be significant in deep water microwave remote sensing but is seldom considered in the surf zone. Keller and Wright (1976) [82] propose a correction of Bragg speeds of $\pm 3\%$ of the $U_{10}$ wind speed projected onto the wave direction. Imposing a surface current of $3\%$ has been applied previously to attempt to adjust Doppler speed observations [66]. At the same time, wind can increase the backscattered power, either by increasing the amplitude of small and intermediate scale waves, i. e. waves that are longer than the Bragg waves but shorter than the resolved long waves [30], [34], [40], [78], [83], [84], or by enhancing steepness limited wave breaking [85]. In addition, wind direction affects scattering by inducing wave asymmetry, whereby upwind conditions lead to steepening wave fronts toward the radar antenna [84], [86]. Just like the longer waves, these waves steepen and break, increasing the backscatter and shifting the Doppler speeds [78], [87]. This will also result in a wind direction dependent percentage of (sub-resolution) shadowed regions potentially resulting in different biases for intensity and Doppler speed. In the surfzone, offshore wind (typically downwind relative to the antenna) has nearly zero fetch to develop intermediate scale waves. Hence the influence of the wind direction is not directly transferable from offshore measurements.

While the radar community has a long tradition on studying differences for up-wind and downwind measurements in offshore locations by the influence of small scale features, the effect of wind in the altering of the shape of the long waves has recently gained attention in nearshore studies outside the radar community. Wind can affect the local steepness of the long gravity waves as well, and it can also modulate the position of the breaking point (e.g. Feddersen et al. 2023 [13]). Feddersen et al. (2023) [13] used artificially generated gravity waves, only allowing the wind to act over a limited distance and yet the effect on the wave shape was discernible for wind speeds as low as $U \propto 0.7\ C$, consistent with the discrimination used here (see Eq. 3). In addition, a numerical study performed by Zdyrski and Feddersen [3] shows a steepening of the front face of a solitary wave when affected by offshore wind, thus increasing wave asymmetry. Onshore wind caused the opposite effect, but it enhanced wave growth and wave speed. Both onshore and offshore conditions led to the development of a bound, dispersive wave tail, that would signify additional variations of surface slope.

The occurrence of one or several of the described effects appear to be supported by the present results. Fig. 9 shows histograms where cases of opposing wind have been highlighted, separated by range domains. For two cases, offshore and mid range locations (panels b and c), the opposing wind conditions concentrate towards the smaller, or even

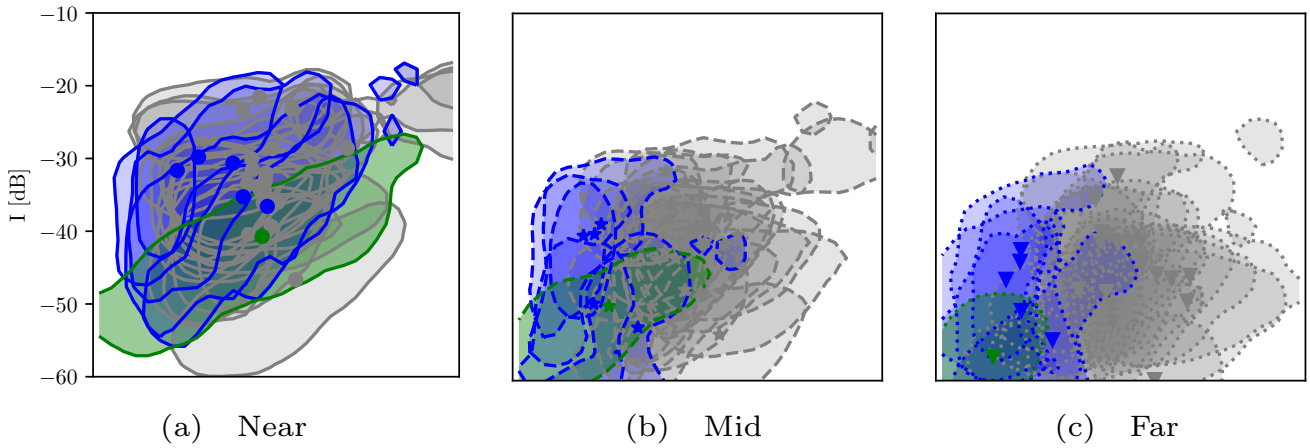


Fig. 9. Histogram contours and centroids of the peak NRCS and according Doppler speed values. Highlighted cases correspond to when the wind blows against the waves. The selected cases are colored according to the dataset (DUCK-I: blue, DUCK-II: green). The cases not fulfilling the criterion are shown in comparison to the rest of the cases (gray).

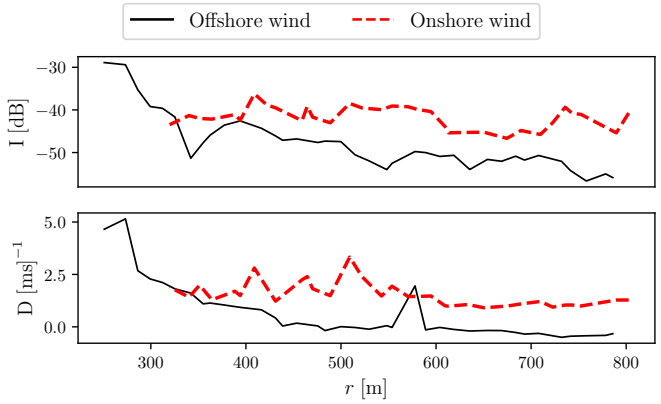


Fig. 10. The evolution of the radar backscatter along wave tracks of different sea states is represented by envelopes. These are constructed by connecting the values at the intensity peak for each time step. The selected sea states (case 16 and 12 from DUCK-II) have similar $\epsilon$, $kh$ and Ur but differ in the wind direction: offshore wind (black) and onshore wind (red) (as defined in Eq. 3).

negative, Doppler speeds, while exhibiting a large spread of NRCS. At closer ranges, the wind effect appears to be reduced. Fig. 10 expounds further on the range dependent influence of the wind direction. When comparing all cases, the wide range of local depth, steepness and Ursell number obscures the analysis, hence two representative examples were selected that share similar values of $\epsilon$, $kh$ and Ur: case 14 (dashed red line, onshore wind) and case 16 (black solid line, offshore wind). The evolution of the NRCS (top panel) and Doppler speed (bottom panel) are represented by the tracked peak intensity at each time step (as explained in sec. II-C). The offshore wind condition exhibits low NRCS and Doppler speed at far range, which gradually increase in magnitude as the wave propagates towards the radar, reaching high NRCS and Doppler speed values at near ranges. In contrast, the NRCS and Doppler speed for onshore wind cases both start from higher values and only slightly increase during propagation. As mentioned already, steep and breaking waves are known to increase the backscatter and Doppler speeds [78], [87]. Lee et al. [78] even concluded that, at low grazing angles, the radar sees mainly the tips of such submeter-scale breaking waves. Discriminating small breakers from steep local slopes is difficult as whitecaps only partially fill the radar cell, leading to similar backscatter values. The impact of small breakers (as a non-Bragg effect) and local slope (as a Bragg effect) grows with increasing range and lower grazing angle. This effect is expected to contribute to the relatively high Doppler speed values in the mid and far range during onshore wind conditions in Fig. 10. In contrast to that, gradual shoaling with less micro– breaking is expected for the offshore wind condition shown, which could explain the gradual increase of both Doppler speed and intensity.

The present observations can be interpreted as consistent with some of the mechanisms described above. Increased wave asymmetry at several scales, including the longer gravity waves, could explain larger NRCS and Doppler speeds for onshore wind conditions, and the opposite for offshore wind con-

ditions. A numerical model of non-linear wave evolution and a suited backscatter model of the resulting microwave backscatter would be beneficial to test these hypotheses. However, the interaction mechanisms between wind and waves have been largely neglected in past and present numerical studies, that rely mainly on variations of the Boussinesq equation to model shallow water waves and related phenomena. Recent breaking studies such as [2] focus solely on the wave shape and the sloping angle of the beach in their scaling laws. The results shown here suggest that wind has a considerable effect on the kinematics of the waves and must therefore be incorporated in nearshore studies, both in field campaigns and numerical studies.

We also explored some indications of radar system specific aspects influencing the backscatter. Since we did not yet investigate these effects comprehensively enough to draw definitive conclusions on their origins and consequences we only summarize them briefly here. The moments of Doppler speed –intensity histograms for breaking waves were similar for all cases, with the exception of apparently higher backscatter in the far range when the range spreading loss is removed. Comparisons to the uncorrected data (see Supplementary Material) indicates a possible saturation of a few individual pulses within a chunk of pulses used to compute the intensity and Doppler speed. This would complicate attempts to infer details about the roller size, shape, structure, or amount of droplets and spray from the backscatter. Increasing the chunk size, or the time required to obtain a Doppler speed estimate, was also found to lower the spread of the obtained values. Pulse smearing effects [23] were found to affect the spatial structure of the signal, especially at the rear side of the waves (facing away from the radar). Investigating on these system-dependent effects is relevant because it could affect radar-derived assessments, such as the inversion of waves from radar images, which implicitly assume that the radar signal is mostly dependent on free surface features [56], [88], [89]. We will address these effects in greater detail within a numerical study that is currently in preparation.

## V. Conclusion

Coherent X-band radars have the potential to detect the influence of environmental conditions on the shoaling and breaking in the nearshore. Significant sensitivity was found for several hydrodynamic and environmental parameters. However, the main conclusion is that it is the combined interaction of those parameters that guides the wave kinematics. The results are consistent for two radar systems operated at two sites. The data was processed by three main approaches: First, the analysis of the backscatter was reduced to data points extracted at the front of waves where the intensity peaks. Second, the impact of the environment and sea states was depicted through conditional Doppler speed–Intensity ($D$-$I$) histograms, which present the statistics over range sections. Third, automatic wave tracking illustrates the wave kinematics transitioning from the outer surf zone to the shore.

The $D$–$I$ evolution tracks follow different patterns depending on hydrodynamic and environmental conditions. In particular the wind direction has a significant effect on the shape of the backscatter evolution along the wave track. During offshore blowing wind conditions, the intensity and the Doppler speed start from lower values but increase more rapidly while for onshore winds the Doppler speed and intensity start from higher values and grow less.

The shape of the $D$–$I$ tracks also determines the characteristics of the histograms. The wave kinematics for given conditions are reflected in the position and extent along the normalized Doppler speed and intensity axes and, more importantly, in the associated rate of change of the values. A comparison of histograms sorted according to a multitude of parameters suggests that the Ursell number, calculated at the outermost observation point, is well suited to classify the radar backscatter. Cases with high Ursell number exhibit elongated, nearly straight histograms where the increase in intensity appears to be proportional to the increase in Doppler speed. The proportionality is altered by the wind conditions, with offshore winds resulting in less Doppler speed increase, and onshore winds resulting in more. We conclude that when disregarding the wind effects, the radar observations are in agreement with the shallow water theory where the Ursell number defines the dominating terms in governing equation, that is the Boussinesq equation. It remains to be investigated how the wind alters the balance between shape and acceleration that is expressed by the equation.

The distinct impact of wave steepness and the relative depth and wind found herein match previous findings. In contrast to prior research, where the focus was on localized effects close to the breaking point, this study tracked the wave evolution over the course of 500 m and beyond and shows that hydrodynamic parameters and wind affect the process in a more global sense.

To confirm the implication of the observations, the possible role of the imaging mechanism must be investigated. Although backscattering models are available, they are not suited to shed light on the non-linear nearshore kinematics observed under grazing incidence conditions. During the analysis of the data, we compared the data with simulated radar backscatter of shoaling waves. This material will be the subject of future work. The advantage of simulations is that the shape of the sea surface is known and different imaging mechanisms can be compared. The presented observations are crucial in validating the implementation of a suitable radar model.

If the distinct patterns of NRCS and Doppler speed can be related to the local wave steepness and the radial velocity, coherent marine radars can be used to characterize the wave evolution from the outer surf zone to the shore as a function of wind and wave conditions. This requires an investigation of the influence of additional imaging mechanisms that may hamper the dominance of tilt modulation.

## REFERENCES


[1] X. Barthelemy, M. Banner, W. Peirson, F. Fedele, M. Allis, and F. Dias, "On a unified breaking onset threshold for gravity waves in deep and intermediate depth water," *Journal of Fluid Mechanics*, vol. 841, pp. 463–488, 2018.

[2] W. Mostert and L. Deike, "Inertial energy dissipation in shallow-water breaking waves," *Journal of Fluid Mechanics*, vol. 890, 2020.

[3] T. Zdyrski and F. Feddersen, "Wind-induced changes to surface gravity wave shape in shallow water," *Journal of Fluid Mechanics*, vol. 913, p. A27, 2021. [Online]. Available: https://doi.org/10.1017/jfm.2021.15

[4] F. C. Ting and J. T. Kirby, "Dynamics of surf-zone turbulence in a strong plunging breaker," *Coastal Engineering*, vol. 24, no. 3-4, pp. 177–204, 1995. [Online]. Available: https://doi.org/10.1016/0378-3839(94)00036-W

[5] ——, "Dynamics of surf-zone turbulence in a spilling breaker," *Coastal Engineering*, vol. 27, no. 3-4, pp. 131–160, 1996. [Online]. Available: https://doi.org/10.1016/0378-3839(95)00037-2

[6] C. Blenkinsopp and J. Chaplin, "Void fraction measurements in breaking waves," *Proceedings of the Royal Society A: Mathematical, Physical and Engineering Sciences*, vol. 463, no. 2088, pp. 3151–3170, 2007.

[7] H. Chanson and L. Jaw-Fang, "Plunging jet characteristics of plunging breakers," *Coastal Engineering*, vol. 31, no. 1-4, pp. 125–141, 1997. [Online]. Available: https://doi.org/10.1016/S0378-3839(96)00056-7

[8] T. Yasuda, H. Mutsuda, N. Mizutani, and H. Matsuda, "Relationships of plunging jet size to kinematics of breaking waves with spray and entrained air bubbles," *Coastal engineering journal*, vol. 41, no. 3-4, pp. 269–280, 1999. [Online]. Available: https://doi.org/10.1142/S0578563499000164

[9] G. Bullock, C. Obhrai, D. Peregrine, and H. Bredmose, "Violent breaking wave impacts. Part 1: Results from large-scale regular wave tests on vertical and sloping walls," *Coastal Engineering*, vol. 54, no. 8, pp. 602–617, 2007. [Online]. Available: https://doi.org/10.1016/j.coastaleng.2006.12.002

[10] T. Aagaard, M. G. Hughes, and G. Ruessink, "Field observations of turbulence, sand suspension, and cross-shore transport under spilling and plunging breakers," *Journal of Geophysical Research: Earth Surface*, vol. 123, no. 11, pp. 2844–2862, 2018. [Online]. Available: https://doi.org/10.1029/2018JF004636

[11] S. Mead and K. Black, "Predicting the breaking intensity of surfing waves," *Journal of Coastal Research on Surfing. Special Issue 29*, pp. 51–65, 2001.

[12] A. O'Dea, K. Brodie, and S. Elgar, "Field observations of the evolution of plunging-wave shapes," *Geophysical Research Letters*, vol. 48, no. 16, p. e2021GL093664, 2021. [Online]. Available: https://doi.org/10.1029/2021GL093664

[13] F. Feddersen, A. M. Fincham, K. L. Brodie, A. P. Young, M. Spydell, D. J. Grimes, M. Pieszka, and K. Hanson, "Cross-shore wind-induced changes to field-scale overturning wave shape," *Journal of Fluid Mechanics*, vol. 958, Feb. 2023.

[14] G. R. Valenzuela, "Theories for the interaction of electromagnetic and oceanic waves—A review," *Boundary-Layer Meteorology*, vol. 13, no. 1-4, pp. 61–85, 1978.

[15] S. Støle-Hentschel, J. Seemann, J. C. Nieto Borge, and K. Trulsen, "Consistency between sea surface reconstructions from nautical X-band radar Doppler and amplitude measurements," *Journal of Atmospheric and Oceanic Technology*, vol. 35, no. 6, pp. 1201–1220, 2018.

[16] B. L. Lewis and I. D. Olin, "Experimental study and theoretical model of high-resolution radar backscatter from the sea," *Radio Science*, vol. 15, no. 04, pp. 815–828, 1980.

[17] O. Phillips, "Radar returns from the sea surface—Bragg scattering and breaking waves," *Journal of physical oceanography*, vol. 18, no. 8, pp. 1065–1074, 1988.

[18] J. M. Smith, E. M. Poulter, and J. A. McGregor, "Doppler radar measurements of wave groups and breaking waves," *Journal of Geophysical Research*, vol. 101, no. C6, pp. 14 269–14 282, 1996.

[19] P. A. Hwang, M. A. Sletten, and J. V. Toporkov, "Breaking wave contribution to low grazing angle radar backscatter from the ocean surface," *Journal of Geophysical Research*, vol. 113, p. C09017, 2008.

[20] E. M. Poulter, M. J. Smith, and J. A. McGregor, "Microwave backscatter from the sea surface: Bragg scattering by short gravity waves," *Journal of Geophysical Research: Oceans*, vol. 99, no. C4, pp. 7929–7943, 1994.

[21] M. C. Haller and D. R. Lyzenga, "Comparison of radar and video observations of shallow water breaking waves," *IEEE transactions on geoscience and remote sensing*, vol. 41, no. 4, pp. 832–844, 2003.

[22] P. A. Catalán, M. C. Haller, and W. J. Plant, "Microwave backscattering from surf zone waves," *Journal of Geophysical Research: Oceans*, vol. 119, no. 5, pp. 3098–3120, 2014.

[23] M. Streßer, J. Seemann, R. Carrasco, M. Cysewski,

J. Horstmann, B. Baschek, and G. Deane, "On the interpretation of coherent marine radar backscatter from surf zone waves," *IEEE Transactions on Geoscience and Remote Sensing*, 2022.

[24] L. Wetzel, "On microwave scattering by breaking waves," in *Wave dynamics and radio probing of the ocean surface*. Springer, 1986, pp. 273–284.

[25] W. Melville, M. R. Loewen, F. C. Felizardo, A. T. Jessup, and M. Buckingham, "Acoustic and microwave signatures of breaking waves," *Nature*, vol. 336, no. 6194, pp. 54–56, Nov. 1988.

[26] E. A. Ericson, D. R. Lyzenga, and D. T. Walker, "Radar backscatter from stationary breaking waves," *Journal of Geophysical Research*, vol. 104, no. C12, pp. 29 679–29 695, Dec. 1999.

[27] M. A. Sletten, J. C. West, X. Liu, and J. H. Duncan, "Radar investigations of breaking water waves at low grazing angle with simultaneous high-speed optical imagery," *Radio Science*, vol. 38, no. 6, p. 1110, 2003.

[28] P. A. Catalán, M. C. Haller, R. A. Holman, and W. J. Plant, "Optical and microwave detection of wave breaking in the surf zone," *IEEE Transactions on Geoscience and Remote Sensing*, vol. 49, no. 6, pp. 1879–1893, 2011.

[29] W. J. Plant, W. C. Keller, and J. W. Wright, "Modulation of coherent microwave backscatter by shoaling waves," *J. Geophys. Res.*, vol. 83, no. C3, pp. 1347–1352, Mar. 1978.

[30] W. J. Plant, "A model for microwave Doppler sea return at high incidence angles: Bragg scattering from bound, tilted waves," *Journal of Geophysical Research*, vol. 102, no. C9, pp. 21,131–21,146, 1997.

[31] A. T. Jessup, W. K. Melville, and W. C. Keller, "Breaking waves affecting microwave backscatter: 1. Detection and verification," *Journal of Geophysical Research*, vol. 96, no. C11, p. 20547, 1991. [Online]. Available: http://doi.wiley.com/10.1029/91JC01993

[32] J. Wright, "A new model for sea clutter," *IEEE Transactions on Antennas and Propagation*, vol. 16, no. 2, pp. 217–223, 1968.

[33] W. Alpers and K. Hasselmann, "Spectral signal to clutter and thermal noise properties of ocean wave imaging synthetic aperture radars," *International Journal of Remote Sensing*, vol. 3, pp. 423–446, 1982.

[34] R. Romeiser, A. Schmidt, and W. Alpers, "A three-scale composite surface model for the ocean wave-radar modulation transfer function," *Journal of Geophysical Research*, vol. 99, no. C5, pp. 9785–9801, 1994.

[35] F. A. Bertrand Chapron, Fabrice Collard, "Direct measurements of ocean surface velocity from space: Interpretation and validation," *Journal of Geophysical Research: Oceans*, vol. 110, 2005.

[36] Y. Yurovsky, V. Kudryavtsev, S. Grodsky, and B. Chapron, "Sea surface Ka-band doppler measurements: Analysis and model development," *Remote Sensing*, vol. 11, no. 7, p. 839, Apr. 2019. [Online]. Available: https://www.mdpi.com/2072-4292/11/7/839

[37] F. Polverari, A. Wineteer, E. Rodriguez, D. Perkovic-Martin, P. Siqueira, J. T. Farrar, M. Adam, M. C. Tarrés, and J. B. Edson, "A Ka-band wind geophysical model function using doppler scatterometer measurements from the air-sea interaction tower experiment," *Remote Sensing*, vol. 14, no. 9, p. 2067, Apr. 2022.

[38] W. J. Plant, W. C. Keller, K. Hayes, and G. Catham, "Normalized radar cross section of the sea for backscatter: 1. Mean levels," *Journal of Geophysical Research*, vol. 115, no. C09032, 2010.

[39] W. J. Plant and V. Irisov, "A joint active/passive physical model of sea surface microwave signatures," *Journal of Geophysical Research: Oceans*, vol. 122, no. 4, pp. 3219–3239, Apr. 2017. [Online]. Available: http://doi.wiley.com/10.1002/2017JC012749

[40] D. Miret, G. Soriano, F. Nouguier, P. Forget, M. Saillard, and C.-A. Guerin, "Sea surface microwave scattering at extreme grazing angle: Numerical investigation of the doppler shift," *IEEE Transactions on Geoscience and Remote Sensing*, vol. 52, no. 11, pp. 7120–7129, Nov. 2014.

[41] J. V. Toporkov and M. A. Sletten, "Statistical properties of low-grazing range-resolved sea surface backscatter generated through two-dimensional direct numerical simulations," *IEEE Transactions on Geoscience and Remote Sensing*, vol. 45, no. 5, pp. 1181–1197, May 2007.

[42] F. Bass, I. Fuks, A. Kalmykov, I. Ostrovsky, and A. Rosenberg, "Very high frequency radiowave scattering by a disturbed sea surface Part I: Scattering from a slightly disturbed boundary," *IEEE Transactions on Antennas and Propagation*, vol. 16, no. 5, pp. 554–559, 1968.

[43] D. B. Trizna, "A model for Brewster angle damping and multipath effects on the microwave radar sea echo at low grazing angles," *IEEE Transactions on Geoscience and Remote Sensing*, vol. 35, no. 5, pp. 1232–1244, 1997.

[44] R. Holman and M. C. Haller, "Remote sensing of the nearshore," *Annual Review of Marine Science*, vol. 5, pp. 95–113, 2013.

[45] M. C. Senet, J. Seemann, and F. Ziemer, "The near-surface current velocity determined from image sequences of the sea surface," *IEEE Transactions on Geoscience and Remote Sensing*, vol. 39, no. 3, pp. 492–505, 2001.

[46] B. Lund, B. K. Haus, H. C. Graber, J. Horstmann, R. Carrasco, G. Novelli, C. M. Guigand, S. Mehta, N. J. M. Laxague, and T. M. Özgökmen, "Marine X-band radar currents and bathymetry: an argument for a wave number-dependent retrieval method," *Journal of Geophysical Research: Oceans*, vol. 125, no. 2, Feb. 2020.

[47] D. A. Honegger, M. C. Haller, and R. A. Holman, "High-resolution bathymetry estimates via X-band marine radar: 2. Effects of currents at tidal inlets," *Coastal Engineering*, vol. 156, no. December 2019, p. 103626, 2020.

[48] P. Chernyshov, T. Vrecica, M. Streßer, R. Carrasco, and Y. Toledo, "Rapid wavelet-based bathymetry inversion method for nearshore X-band radars," *Remote Sensing of Environment*, vol. 240, no. January, p. 111688, 2020. [Online]. Available: https://doi.org/10.1016/j.rse.2020.111688

[49] J. Atkinson, L. S. Esteves, J. J. Williams, P. S. Bell, and D. L. McCann, "Nearshore monitoring with x-band radar: Maximizing utility in dynamic and complex environments," *Journal of Geophysical Research: Oceans*, vol. 126, no. 4, Apr. 2021.

[50] M. Streßer and J. Horstmann, "Remote quantification of nearshore wave energy dissipation rates from coherent x-band radar backscatter," in *2019 IEEE/OES Twelfth Current, Waves and Turbulence Measurement (CWTM)*. IEEE, 2019, pp. 1–6.

[51] M. Streßer, J. Horstmann, and B. Baschek, "Surface wave and roller dissipation observed with shore-based doppler marine radar," *Journal of Geophysical Research: Oceans*, vol. 127, no. 8, p. e2022JC018437, 2022.

[52] J. A. Puleo, G. Farquharson, S. J. Frasier, and K. T. Holland, "Comparison of optical and radar measurements of surf and swash zone velocity fields," *Journal of Geophysical Research: Oceans*, vol. 108, no. C3, 2003.

[53] D. Perkovic, T. C. Lippmann, and S. J. Frasier, "Longshore surface currents measured by Doppler radar and video PIV techniques," *IEEE Transactions on Geoscience and Remote Sensing*, vol. 47, no. 8, pp. 2787–2800, Aug. 2009.

[54] M. C. Haller, D. Honegger, and P. A. Catalán, "Rip current observations via marine radar," *Journal of Waterway, Port, Coastal, and Ocean Engineering*, vol. 140, no. 2, pp. 115–124, Mar. 2014.

[55] D. A. Honegger, M. C. Haller, W. R. Geyer, and G. Farquharson, "Oblique internal hydraulic jumps at a stratified estuary mouth," *Journal of Physical Oceanography*, vol. 47, no. 1, pp. 85–100, Jan. 2017.

[56] A. J. Simpson, F. Shi, J. T. Jurisa, D. A., T.-J. Hsu, and M. C. Haller, "Observations and modeling of a buoyant plume exiting into a tidal cross-flow and exhibiting along-front instabilities," *Journal of Geophysical Research: Oceans*, vol. 127, no. 2, Feb. 2022.

[57] I. S. Robinson, N. P. Ward, C. P. Gommenginger, and M. A. Tenorio-Gonzales, "Coastal oceanography applications of digital image data from marine radar," *Journal of Atmospheric and Oceanic Technology*, vol. 17, pp. 721–735, 2000.

[58] G. Farquharson, S. J. Frasier, B. Raubenheimer, and S. Elgar, "Surf zone surface displacement measurements using interferometric microwave radar," in *2010 IEEE International Geoscience and Remote Sensing Symposium*. IEEE, Jul. 2010.

[59] D. J. McLaughlin, N. Allan, E. M. Twarog, and D. B. Trizna, "High resolution and polarimetric radar and scattering and measurements of low and grazing angle and sea clutter," *IEEE Journal of Oceanic Engineering*, vol. 20, no. 3, pp. 166–178, Jul. 1995.

[60] D. B. Trizna and D. J. Carlson, "Studies of dual polarized low grazing angle radar sea scatter in nearshore regions," *IEEE Transactions on Geoscience and Remote Sensing*, vol. 34, no. 3, pp. 747–757, May 1996.

[61] S. J. Frasier and R. E. McIntosh, "Observed wavenumber-frequency properties of microwave backscatter from the ocean surface at near-grazing angles," *Journal of Geophysical Research*, vol. 101, no. C8, pp. 18,391, 1996.

[62] C. L. Rino, E. Eckert, A. Siegel, T. Webster, andy Ochadlick, M. Rankin, and J. Davis, "X-band low-grazing-angle ocean backscatter obtained during LOGAN 1993," *IEEE Journal of Oceanic Engineering*, vol. 22, no. 1, pp. 18–26, Jan. 1997.

[63] C. L. Stevens, M. Poulter, M. J. Smith, and J. A. McGregor, "Nonlinear features in wave-resolving microwave radar observations of ocean waves," *Journal of Oceanic Engineering*, vol. 24, no. 4, pp. 470–480, Oct. 1999.

[64] P. Forget, M. Saillard, and P. Broche, "Observations of the sea surface by coherent L band radar at low grazing angles in a nearshore environment," *Journal of Geophysical Research*, vol. 111, p. C09015, 2006.

[65] R. E. McIntosh, S. J. Frasier, and J. B. Mead, "FOPAIR: A focused array imaging radar for ocean remote sensing," *IEEE Transactions on Geoscience and Remote Sensing*, vol. 33, no. 1, pp. 115–124, 1995.

[66] G. Farquharson, S. J. Frasier, B. Raubenheimer, and S. Elgar, "Microwave radar cross sections and Doppler velocities measured in the surf zone," *Journal of Geophysical Research: Oceans*, vol. 110, no. C12, p. C12024, 2005.

[67] W. J. Plant, W. C. Keller, and K. Hayes, "Measurement of river surface currents with coherent microwave systems," *IEEE Transactions on Geoscience and Remote Sensing*, vol. 43, no. 6, pp. 1242–1257, Jun. 2005.

[68] J. Horstmann, J. Bödewadt, R. Carrasco, M. Cysewski, J. Seemann, and M. Streßer, "A coherent on receive X-band marine radar for ocean observations," *Sensors*, vol. 21, no. 23, p. 7828, Nov. 2021. [Online]. Available: https://www.mdpi.com/1424-8220/21/23/7828

[69] C. P. Gommenginger, N. P. Ward, G. J. Fisher, I. S. Robinson, and S. R. Boxall, "Quantitative Microwave Backscatter Measurements from the Ocean Surface Using Digital Marine Radar Images," *Journal of Atmospheric and Oceanic Technology*, vol. 17, pp. 665–678, 2000.

[70] M. Streßer, C. O. Collins, B. Lund, J. Humbertson, J. Horstmann, R. Carrasco, N. J. Spore, and K. L. Brodie, "Coherent Marine X-band Radar Deployment during DUNEX," U.S. Army Engineer Research and Development Center, Coastal and Hydraulics Laboratory, Technical Report, 2023, in press.

[71] S. Dick, E. Kleine, S. H. Müller-Navarra, H. Klein, H. Komo, S. Dick, E. Kleine, S. H. Müller-Navarra, H. Klein, and H. C. N. Komo, "The operational circulation model of BSH(BSHcmod): Model description and validation," Bundesamt für Seeschifffahrt und Hydrographie, Hamburg, Tech. Rep. 29/2001, 2001, berichte des Bundesamtes für Seeschifffahrt und Hydrographie.

[72] P. Catalán and M. Haller, "Remote sensing of breaking wave phase speeds with application to nonlinear depth inversion," *Coastal Engineering*, vol. 55, pp. 93–111, 2008.

[73] I. A. Svendsen, "Wave Heights and Set-up in a Surf Zone," *Coastal Engineering*, vol. 8, pp. 303–329, 1984.

[74] Z. Chen, X. Chen, C. Zhao, J. Li, W. Huang, and E. W. Gill, "Observation and Intercomparison of Wave Motion and Wave Measurement Using Shore-Based Coherent Microwave Radar and HF Radar," *IEEE Transactions on Geoscience and Remote Sensing*, vol. 57, no. 10, pp. 7594–7605, Oct. 2019.

[75] B. Raubenheimer, "Observations and Predictions of Fluid Velocities in the Surf and Swash Zones," *Journal of Geophysical Research*, vol. 107, no. C11, p. 3190, 2002.

[76] Støle-Hentschel, "Tracking the evolution of ocean waves," *Image Processing On Line*, in press 2023. [Online]. Available: https://ipolcore.ipol.im/demo/clientApp/demo.html?id=77777000368

[77] R. Grompone von Gioi and G. Randall, "A sub-pixel edge detector: an implementation of the canny/devernay algorithm," *IPOL Journal-Image Processing On Line, 2017, vol. 7, pp. 347-372*, 2017.

[78] P. Lee, J. Barter, E. Caponi, M. Caponi, C. Hindman, B. Lake, and H. Rungaldier, "Wind-speed dependence of small-grazing-angle microwave backscatter from sea surfaces," *IEEE Transactions on Antennas and Propagation*, vol. 44, no. 3, pp. 333–340, Mar. 1996.

[79] D. H. Peregrine, "Breaking waves on beaches," *Annual Review of Fluid Mechanics*, vol. 15, no. 1, pp. 149–178, 1983. [Online]. Available: https://doi.org/10.1016/j.coastaleng.2006.12.002

[80] S. J. Frasier, Y. Liu, and R. E. McIntosh, "Space-time properties of radar sea spikes and their relation to wind and wave conditions," *Journal of Geophysical Research: Oceans*, vol. 103, no. C9, pp. 18 745–18 757, 1998.

[81] W. J. Plant, "Bragg Scattering of Electromagnetic Waves from the Air/sea Interface," in *Surface Waves and Fluxes*, ser. Environmental Fluid Mechanics, G. Geernaert and W. Plant, Eds. Springer Netherlands, 1990, vol. 8, pp. 41–108.

[82] W. Keller and J. Wright, "Modulation of microwave backscatter by gravity waves in a wave tank," Naval Research Lab Washington DC, Tech. Rep., 1976.

[83] D. Ross and W. L. Jones, "On the relationship of radar backscatter to wind speed and fetch," *Boundary-Layer Meteorology*, vol. 13, no. 1–4, pp. 151–163, Jan. 1978.

[84] K. S. Chen, A. K. Fung, and D. A. Weissman, "A Backscattering Model for Ocean Surface," *IEEE Transactions on Geoscience and Remote Sensing*, vol. 30, no. 4, pp. 811–817, Jul. 1992.

[85] D. B. Ross and V. Cardone, "Observations of oceanic whitecaps and their relation to remote measurements of surface wind speed," *Journal of Geophysical Research*, vol. 79, no. 3, pp. 444–452, 1974.

[86] C. Cox and W. Munk, "Measurement of the roughness of the sea surface from photographs of the sun's glitter," *Journal of the Optical Society of America*, vol. 44, no. 11, pp. 838–850, 1954.
[87] P. Lee, J. D. Barter, K. L. Beach, C. L. Hindman, B. M. Lake, H. Rungaldier, J. Shelton, A. Williams, R. Yee, and H. C. Yuen, "X band microwave backscattering from ocean waves," *Journal of Geophysical Research*, vol. 100, no. C2, pp. 2591–2611, Feb. 1995.
[88] H. Dankert, J. Horstmann, and W. Rosenthal, "Wind- and wave-field measurements using marine X-band radar-image sequences," *IEEE Journal of Oceanic Engineering*, vol. 30, no. 3, pp. 534–542, 2005.
[89] H. Dankert and W. Rosenthal, "Ocean surface determination from X-band radar-image sequences," *Journal of Geophysical Research*, vol. 109, no. C04016, 2004.

## ACKNOWLEDGEMENTS

This work was funded by the European Research Council through the HIGHWAVE project (grant no. 833125). PAC thanks the Centre Borelli at ENS Paris-Saclay for partial funding during a sabbatical term, as well as ANID Project 1523A0009 FONDAP 2023 and ANID PIA/APOYO AFB230003.

We thank the U.S. Army Corps of Engineers Research and Development Center's Field Research Facility for the use of their facility and support of their staff during the 2008 and 2021 field campaigns. Special thanks to Kate Brodie, Tripp Collins, Josh Humberston and Nick Spore for their aid to install and operate the Hereon radar at the FRF in 2021.